Evaluation of the influence of voids on 3D representative volume elements of fiber-reinforced polymer composites using CUF micromechanics

E. Carrera,[*] M. Petrolo,[†] M.H. Nagaraj,[‡] M. Delicata[§]

MUL^2 Group, Department of Mechanical and Aerospace Engineering, Politecnico di Torino
Turin, Italy

Submitted to Composite Structures

Author for correspondence:
Marco Petrolo
MUL^2 Group, Department of Mechanical and Aerospace Engineering,
Politecnico di Torino,
Corso Duca degli Abruzzi 24,
10129 Torino, Italy,
tel: +39 011 090 6845,
fax: +39 011 090 6899,
e-mail: marco.petrolo@polito.it

[*]Professor of Aerospace Structures and Aeroelasticity, erasmo.carrera@polito.it
[†]Associate Professor, marco.petrolo@polito.it
[‡]Ph.D. Student, manish.nagaraj@polito.it
[§]Research Assistant, michele.delicata@polito.it

Abstract

This paper presents numerical results on the micromechanics linear analysis of representative volume elements (RVE) containing voids. The modeling approach is the micromechanical framework within the Carrera Unified Formulation (CUF) in which fibers and matrix are 1D finite elements (FE) with enriched kinematics and component-wise capabilities (CW). RVE models are 3D and consider all six stress components. Such a modeling strategy leads to a twofold reduction of the degrees of freedom (DOF) as compared to 3D FE. The numerical assessments address the influence of the volume fraction and distribution of voids, including comparisons with data from the literature and statistical studies regarding homogenized properties and stress fields. The proposed modeling approach can capture the local effects due to the presence of voids, and, given its computational efficiency, the present framework is promising for nonlinear analysis, such as progressive failure.

Keywords: Voids, micromechanics, CUF, fiber reinforced polymers

1 Introduction

Fiber-reinforced composites are increasingly popular in many engineering fields to provide superior performances as compared to metals [1, 2]. In addition to space and aeronautics industries, the automotive and energy sector are making growing use of these materials due to the lightweight and the high specific strength and stiffness [3, 4]. Composites have a multiscale nature, and the proper detection of fundamental mechanical behavior requires modeling of the various scales. The present paper focuses on the microscale in which the differences between constituent properties and the presence of interfaces and defects lead to modeling challenges [5]. Defects stemming from manufacturing can significantly modify the microscale characteristics and lead to various damage mechanisms, such as [2, 6] interfacial debonding and sliding, matrix microcracking, delamination, fiber breakage, and fiber micro-buckling.

The present paper deals with the numerical modeling of voids in the matrix. Voids can influence the matrix-dominated mechanical properties and lead to the localization of stresses [7]. Many works have investigated the void formation, growth, morphology, and influence on structural performance. The work of Mehdikhani et al. [8] is a comprehensive guide for the selection of these studies.

Computational micromechanics is a popular tool to study defects and related issues. By the direct modeling of the microscale components and defects, micromechanics can provide the homogenized macroscopic mechanical properties and, via de-homogenization, the stress and strain fields at the microscale. Various numerical approaches, e.g., finite elements (FE), can model the microscale via the use of a representative volume element (RVE) containing the typical architecture of the composite structure in hand [9–18]. Other works investigate the effect of voids in the elastic regime and strength prediction, embedding them into the FE model and considering various loading conditions and failure modes [3, 5, 19–30].

The use of FE models can lead to very high computational costs. Such costs may be prohibitive when the 3D structure of the RVE is of interest, or nonlinear analyses are necessary. The present work falls within the Carrera Unified Formulation (CUF) use for micromechanics [31–33]. One of the advantages of CUF is the possibility of modeling multi-component structures as an ensemble of 1D finite elements with enriched cross-section kinematics [34]. Such a capability significantly reduces the computational costs - as there are no aspect ratio constraints - but retains 3D-like accuracy for all stress and strain components. CUF for linear and nonlinear multiscale problems provided twofold reductions on computational costs as compared to 3D FE [35, 36].

The objective of the present work is to investigate the influence of microscale matrix voids on the macroscopic mechanical properties and the microscopic fields. For the first time, CUF is used to model 3D RVE and voids. The modeling of voids includes their volume fraction and distribution. This paper is organized as follows: Sections 2 and 3 describe the theoretical framework for FE and micromechanics, respectively. The numerical results are in Section 4, and conclusions in Section 5.

2 Higher-order 1D structural theories

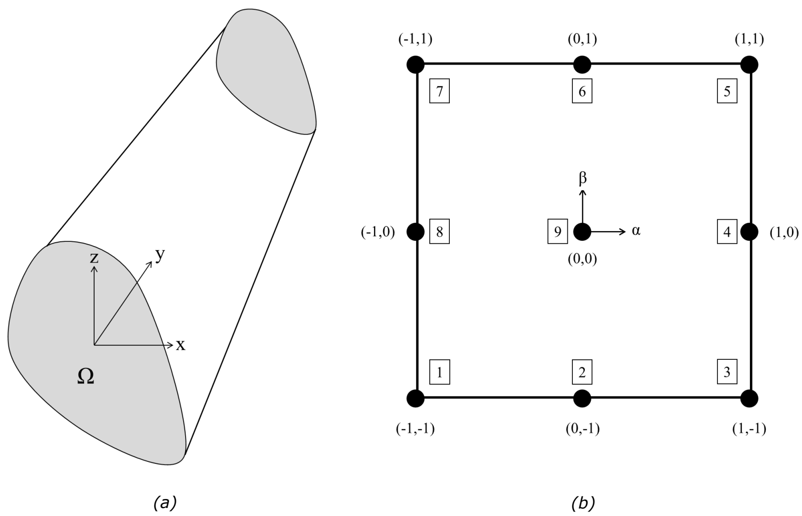

Figure 1: (a) Beam with arbitrary cross-section oriented along the y-axis, and (b) the 9-node bi-quadratic Lagrange expansion element in the natural coordinate system

Considering a beam oriented along the y-axis, as shown in Fig. 1(a), the displacement field in CUF is

$$\mathbf{u} = F_\tau(x,z)\mathbf{u}_\tau(y), \tau = 1, 2, \dots M \tag{1}$$

Where $\mathbf{u}$ is the displacement field and $F_\tau(x,z)$ is the expansion function across the cross-section. $\mathbf{u}_\tau$ is the generalized displacement vector, and M is the number of terms in the expansion function. The choice of F_τ and M is arbitrary. The present work utilizes the Lagrange Expansion (LE) class of expansions to enhance the cross-section kinematics, resulting in a Component-Wise (CW) model. In this approach, Lagrange polynomials explicitly discretize the cross-section geometry and displacement field. This work uses 9-node bi-quadratic expansion elements (L9), see Fig. 1(b), in which the 3D displacement field is

$$
\begin{aligned}
u_x &= \sum_{\tau=1}^{9} F_\tau(x,z) \cdot u_{x_\tau}(y) \\
u_y &= \sum_{\tau=1}^{9} F_\tau(x,z) \cdot u_{y_\tau}(y) \\
u_z &= \sum_{\tau=1}^{9} F_\tau(x,z) \cdot u_{z_\tau}(y)
\end{aligned}
\tag{2}
$$

The use of Lagrange expansion results in a 1D numerical model that explicitly models the 3D domain without the need of fictitious entities like the reference axis. Furthermore, the displacement field consists of only translational degrees of freedom (DOF), without involving rotations. Further details on the use of Lagrange polynomials as expansion functions can be found in [37].

The stress and strain fields in vector notation are

$$
\begin{aligned}
\boldsymbol{\sigma} &= \{\sigma_{xx}, \sigma_{yy}, \sigma_{zz}, \sigma_{xy}, \sigma_{xz}, \sigma_{yz}\}^T \\
\boldsymbol{\epsilon} &= \{\epsilon_{xx}, \epsilon_{yy}, \epsilon_{zz}, \epsilon_{xy}, \epsilon_{xz}, \epsilon_{yz}\}^T
\end{aligned}
\tag{3}
$$

Assuming linear strains, the displacements are related to the strains as

$$
\boldsymbol{\epsilon} = \mathbf{D} \cdot \mathbf{u} \tag{4}
$$

where $\mathbf{D}$ is the linear differentiation operator given by

$$
\mathbf{D} = \begin{bmatrix}
\frac{\partial}{\partial x} & 0 & 0 \\
0 & \frac{\partial}{\partial y} & 0 \\
0 & 0 & \frac{\partial}{\partial z} \\
\frac{\partial}{\partial y} & \frac{\partial}{\partial x} & 0 \\
\frac{\partial}{\partial z} & 0 & \frac{\partial}{\partial x} \\
0 & \frac{\partial}{\partial z} & \frac{\partial}{\partial y}
\end{bmatrix}
$$

The constitutive law, considering an elastic material behavior, is

$$
\boldsymbol{\sigma} = \mathbf{C}\boldsymbol{\epsilon} \tag{5}
$$

where $\mathbf{C}$ is the linear elastic material matrix. The structure is discretized in the axial direction using beam elements, interpolated using the nodal shape functions N_i. The combination of beam elements and cross-section expansions results in a 3D displacement field defined as

$$\mathbf{u}(x, y, z) = F_\tau(x, z) N_i(y) \mathbf{u}_{\tau i} \tag{6}$$

where $\mathbf{u}_{\tau i}$ is the nodal displacement field. Based on the principle of virtual displacements,

$$\delta L_{int} = \delta L_{ext} \tag{7}$$

where δL_{int} is the virtual variation of the internal strain energy,

$$\delta L_{int} = \int_V \delta \boldsymbol{\epsilon}^T \boldsymbol{\sigma} \tag{8}$$

L_{ext} is the work due to the externally applied load,

$$L_{ext} = F_s N_j \delta \mathbf{u}_{sj}^T \mathbf{P} \tag{9}$$

where $\mathbf{P}$ is the external force vector. Using Eqs. (5), (6) and (8), the stiffness matrix is defined as

$$\delta L_{int} = \delta \mathbf{u}_{sj}^T \mathbf{k}_{ij\tau s} \mathbf{u}_{\tau i} \tag{10}$$

with

$$\mathbf{k}_{ij\tau s} = \int_l \int_\Omega \mathbf{D}^T (N_i(y) F_\tau(x, z)) \mathbf{C} \mathbf{D} (N_j(y) F_s(x, z)) \, d\Omega \, dl \tag{11}$$

$\mathbf{k}_{ij\tau s}$ is the 3x3 Fundamental Nucleus (FN), and is invariant with respect to the applied structural theory. Ω and l represent the cross-section domain and beam length, respectively. A detailed explanation of the fundamental nucleus and the assembly of the global stiffness matrix is found in [34].

3 Component-wise micromechanics framework

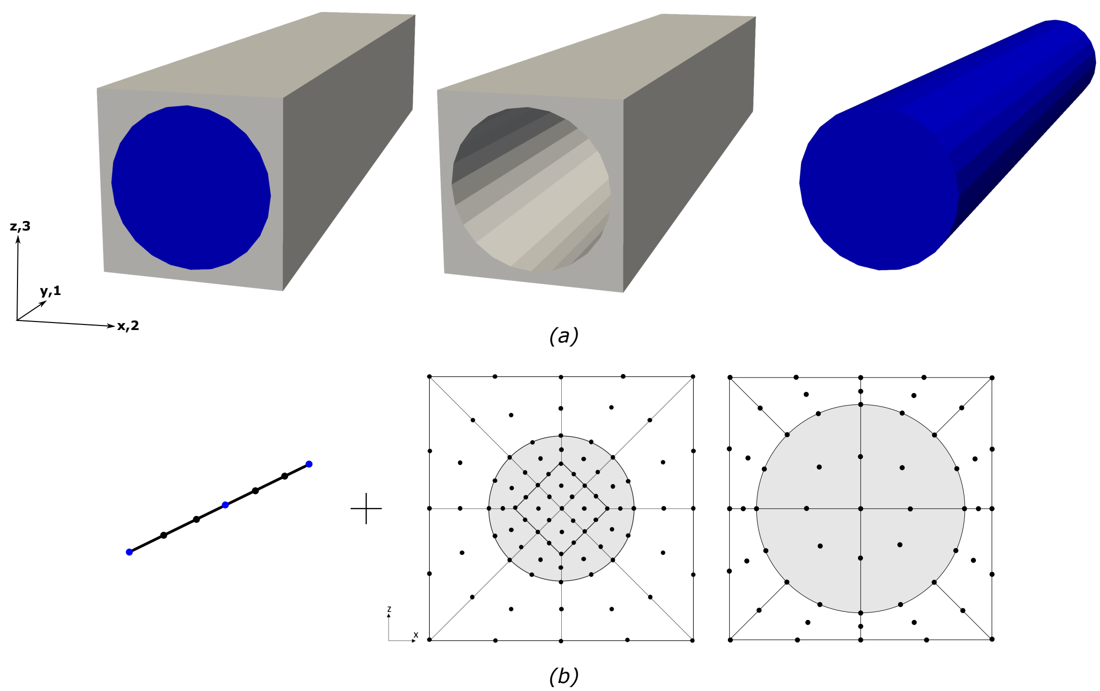

Figure 2: Modelling the RVE using the CW approach. (a) 3D domain of a square-packed RVE and its individual constituents, and (b) 1D-CUF model

The CW micromechanics framework adopts 1D CUF models with Lagrange expansion functions. In this approach, an RVE is modeled, as shown in Fig. 2. Beam elements are used in the RVE thickness direction, and Lagrange expansion elements explicitly model the individual constituents of the RVE cross-section. The formulation is based on the assumption of a periodic microstructure, and periodic boundary conditions (PBC) are applied to the RVE. Such a process ensures the energy equivalence between the heterogeneous material and the effective homogenized medium [9]. The periodic boundary conditions, applied on opposite boundary surfaces, are formulated as

$$u_i^{j+}(x,y,z) - u_i^{j-}(x,y,z) = \bar{\epsilon}_{ik}(x_k^{j+} - x_k^{j-}) \tag{12}$$

where $\bar{\epsilon}_{ik}$ is the applied macroscopic strain, indices $j+$ and $j-$ represent the positive and negative directions, respectively, along x_k. Two PBC sets can thus be distinguished, which are applied in the cross-section edges and the beam ends, respectively, as shown in Fig. 3. The homogenized stress ($\bar{\sigma}_{ij}$)

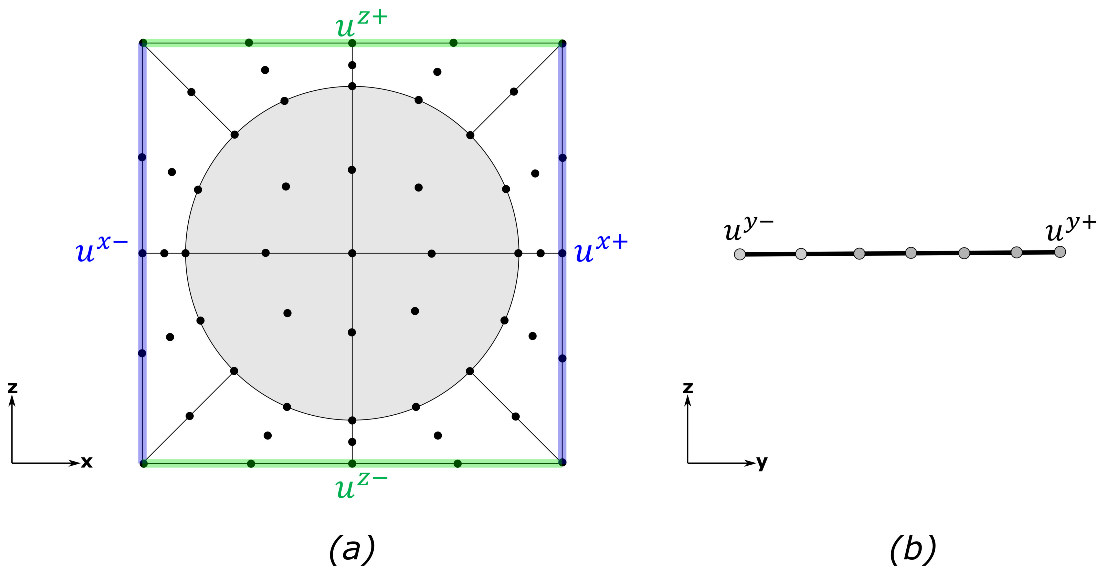

Figure 3: Application of the PBC on a square-packed RVE (a) on the opposite edges of the cross-section and (b) at the beam end nodes

and strain ($\bar{\epsilon}_{ij}$) response is obtained by volume averaging the microscopic fields (σ_{ij}, ϵ_{ij}) [9],

$$\bar{\epsilon}_{ij} = \frac{1}{V}\int_V \epsilon_{ij} dV \tag{13}$$

$$\bar{\sigma}_{ij} = \frac{1}{V}\int_V \sigma_{ij} dV \tag{14}$$

where V is the RVE volume. The constitutive relation for the homogenized medium reads as

$$\bar{\sigma}_{ij} = \bar{C}_{ijkl}\bar{\epsilon}_{ij} \tag{15}$$

where $\bar{C}_{ijkl}$ is the homogenized elastic material matrix. A detailed explanation of the micromechanics framework using the CW approach is given in [31].

Voids are modeled in the matrix constituent of the RVE by selecting a set of Gauss points (GP) within the matrix domain and assigning them arbitrarily low elastic moduli. Such a process creates voids with a domain equal to the volume associated with the selected GP. Matrix GP are iteratively selected as void candidates until the void volume fraction, given as an input, is satisfied. Furthermore, the matrix GP can be selected either randomly throughout the RVE, or be biased in the RVE thickness direction. The former results in voids that are randomly and equally distributed within the RVE, while the latter results in voids clustered towards one end of the RVE. This methodology thus allows for the development of a fully 3D cubic RVE with matrix voids of a required volume fraction as well as morphology. As an example, a multi-fiber RVE with 1% randomly distributed voids has been schematically shown in Fig. 4. Such a technique enables the efficient development of multiple configurations of the RVE for a given void volume fraction, which is an important requirement for statistical studies on the influence of voids.

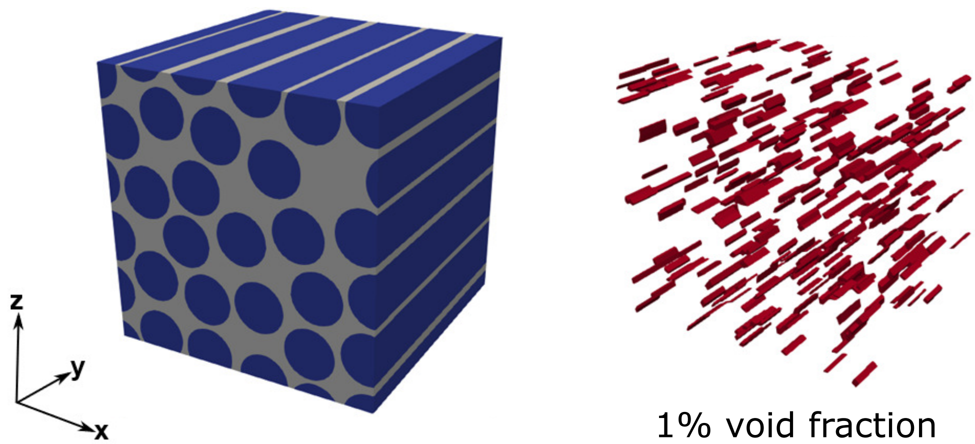

Figure 4: A multi-fibre RVE with 1% voids randomly distributed within the matrix

4 Numerical results

4.1 Pristine RVE

The RVE has 22 randomly distributed fibers, and the material system is carbon/epoxy with 60% of fiber volume fraction. Figure 5 shows the randomly distributed fibers; the blue cylinders represent the carbon fibers, and the white portion indicates the matrix. The side of the cross-section is 38.5 µm. The thickness along the y-axis is 19.25 µm. The radius of the fiber is 3.6 µm. The material properties are in Table 1 and retrieved from Sevenois et al. [38] through a reverse engineering approach. The longitudinal direction of the fiber coincides with the y-axis, see Fig. 2. This section aims to evaluate the influence of the cross-

Table 1: Properties of the constituent materials [38], the units of the elastic moduli are GPa

Material	E_{11}	$E_{22} = E_{33}$	$G_{12} = G_{13}$	G_{23}	$\nu_{12} = \nu_{13}$	ν_{23}
Fiber	223.987	18.534	36.898	7.232	0.258	0.282
Matrix	3.700	3.700	3.700	3.700	0.400	0.400

section modeling on the homogenized properties and select the discretization for all subsequent analyses.

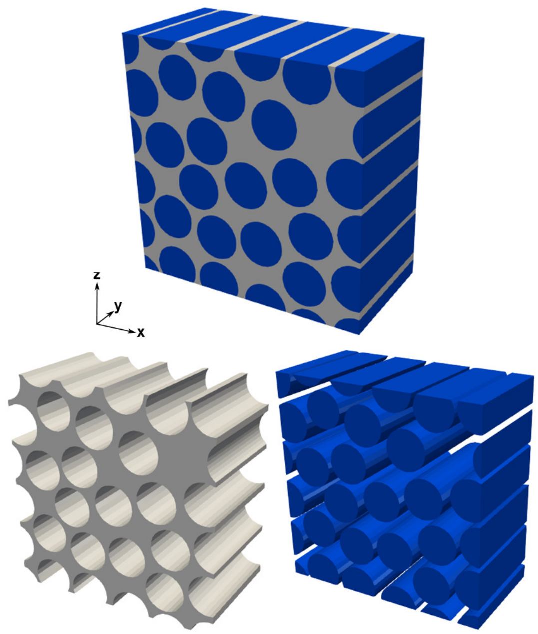

Figure 5: RVE with randomly distributed fibers

Figures 6 show two examples of cross-section discretizations. The FE mesh along y is constant and has one B4 element; as shown in previous works [31, 32], such axial mesh is sufficiently accurate. Figure 7

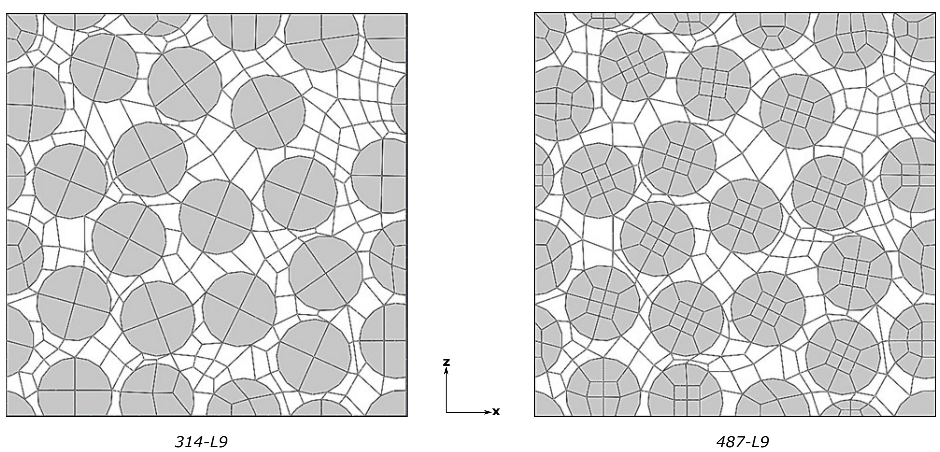

Figure 6: Cross-sections with 314 and 487 L9 elements

shows the homogenized properties for various meshes. The reference value to compute the error is the one provided by the most refined discretization, 3144 L9. The coarsest discretization has the highest error. However, such errors are lower than 2%. Given that the use of the 314 L9 leads to a considerably reduced computational cost for the statistical studies, the following numerical examples will use the same discretization. A further assessment focuses on the verification of the results via a comparison with [38],

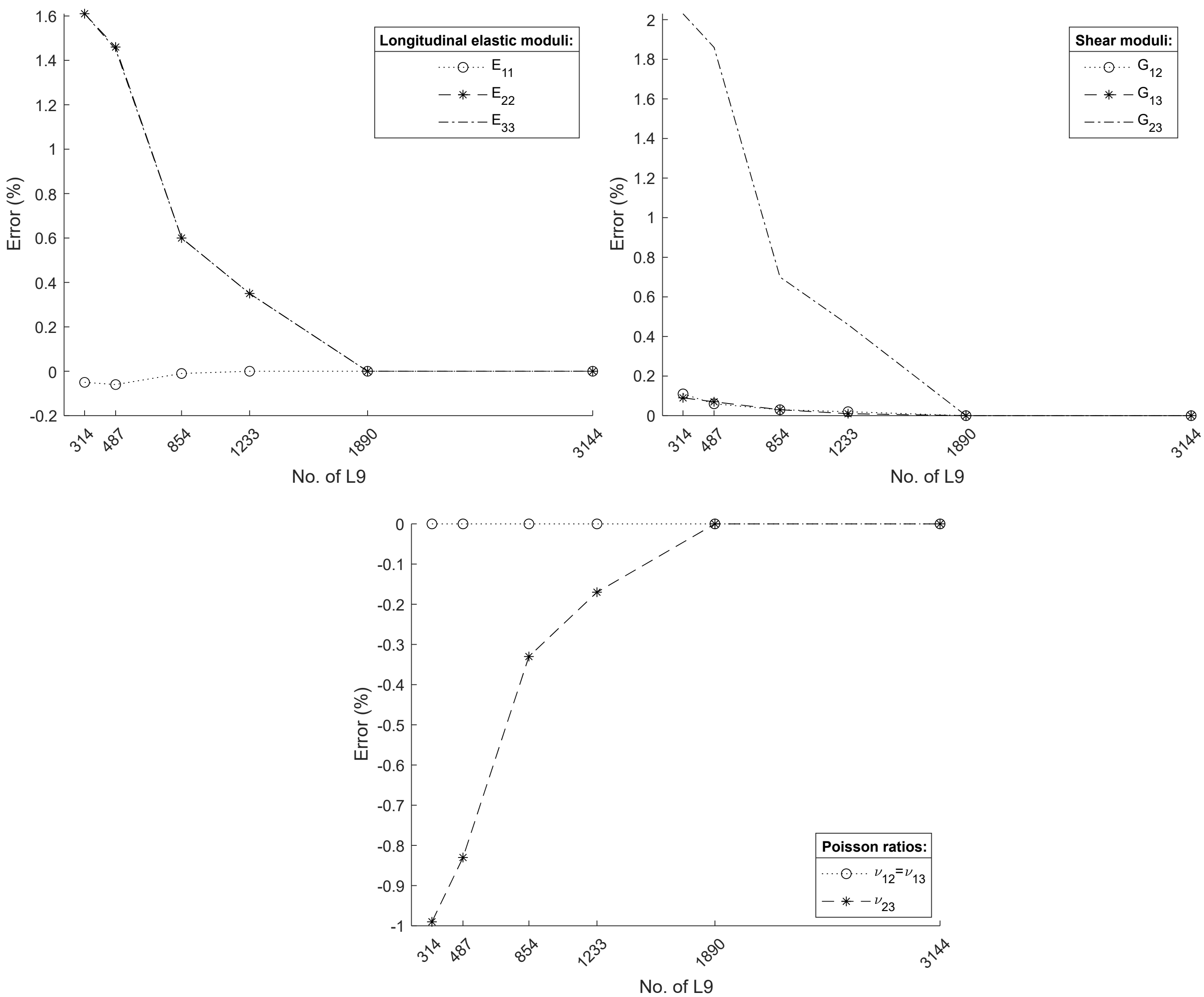

Figure 7: Effect of the cross-section discretization on the homogenized properties of the pristine RVE

see Table 2. The results show a good match. Figures 8 and 9 show stress distributions given by an applied strain of 0.2%.

Table 2: Homogenized properties for the pristine RVE via 314 L9 and results from [38], the units of the elastic moduli are GPa

Model	1D-CUF	FE ref. [38]
E_{11}	135.88	135.74
E_{22}	9.96	9.66
E_{33}	9.91	9.66
G_{12}	5.19	5.31
G_{13}	5.02	5.31
G_{23}	3.15	3.23
ν_{12}	0.31	0.31
ν_{13}	0.31	0.31
ν_{23}	0.47	0.48

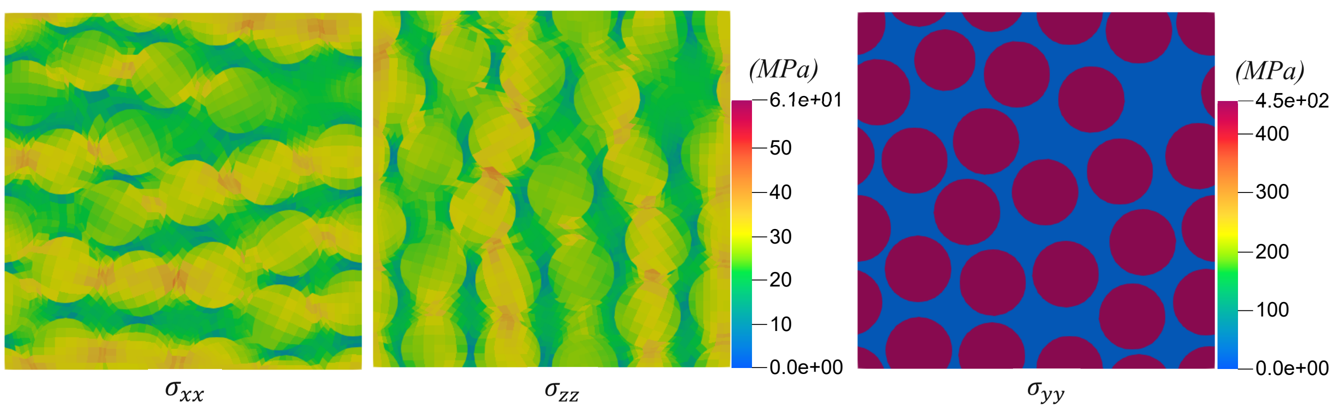

Figure 8: Axial stress contours, σ_{xx}, σ_{zz}, and σ_{yy}, with applied ϵ_{xx}, ϵ_{zz}, and ϵ_{yy}, respectively, pristine RVE

4.2 RVE with voids

The analysis of voids considers two RVE configurations. The first one - referred to as RVE-1, has the same material and geometrical characteristics seen in the previous section. The second one, RVE-2, differs only for the dimension along y; that is, 38.5 µm. From the modeling standpoint, the cross-section discretizations are the same, whereas two B4 are employed in RVE-2. Figure 10 shows both RVE and the beam meshes in which the reported mesh over the matrix is not representative of the numerical model, but it serves postprocessing purposes. o Table 3 summarizes the main characteristics of the models. The shape and void percentages considered in this paper are consistent with those from the literature [8]. The analysis considers two void distributions as follows

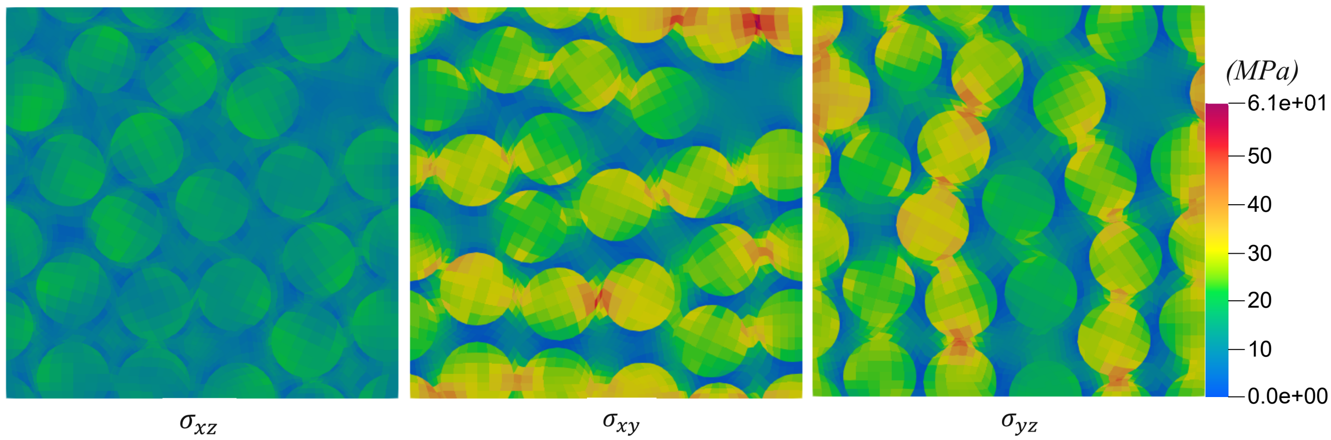

Figure 9: Shear stress contours, σ_{xz}, σ_{xy}, σ_{yz}, with applied ϵ_{xz}, ϵ_{xy}, and ϵ_{yz}, respectively, pristine RVE

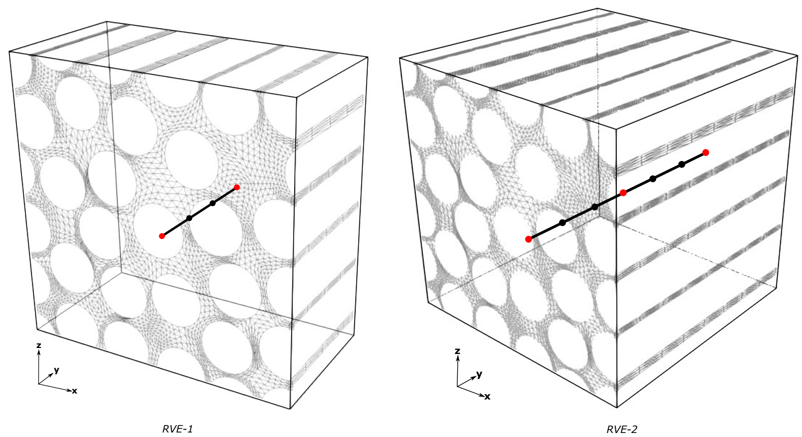

Figure 10: RVE-1 and RVE-2 and beam meshes

- The first distribution - referred to as VD-1 - is random within the RVE. Figure 11 shows an example of this void arrangement for the RVE-2.

- The second distribution - referred to as VD-2 - is random along the cross-section but follows a linear distribution of the void percentage along y. By considering Fig. 12, the first segment along y has 5% of the total voids, while the last one has some 30%. The aim is to simulate a configuration with moderate clustering.

In both cases, 100 distributions per each void volume fraction were considered to evaluate statistical parameters. Table 4 presents the main characteristics of each distribution. VD-2 was applied only to RVE-2 due to the small y-dimension of RVE-1. Furthermore, VD-2 considers the random variation of the slope of the distribution; that is, the maximum of voids can be either on the last segment or the first

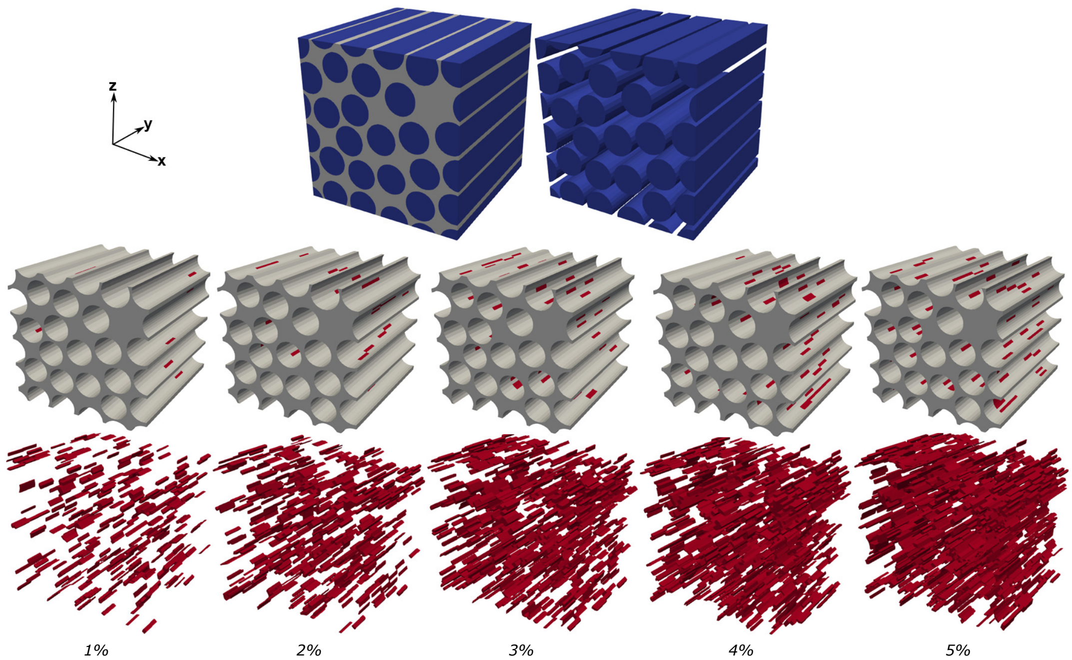

Figure 11: Random distributions of voids with increasing contents, VD-1

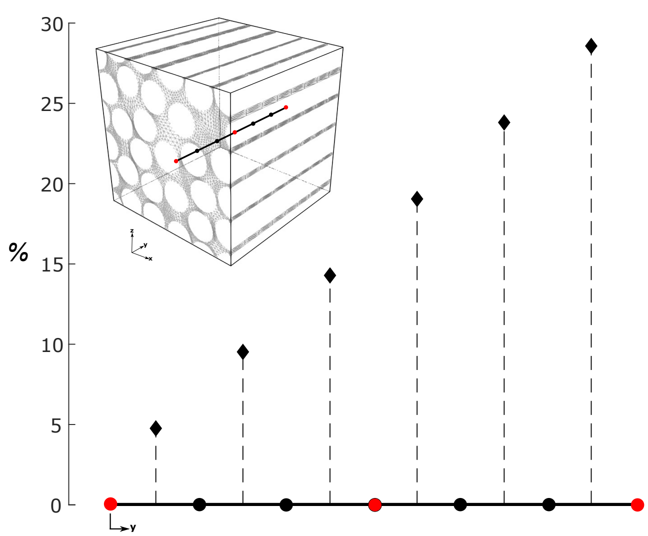

Figure 12: Clustering of voids, VD-2

Table 3: Structural and FE modeling of RVE-1 and RVE-2

	Discretization	DOF
RVE-1	314 L9 on the cross-section, one B4 along y	15876
RVE-2	314 L9 on the cross-section, two B4 along y	27783

one. The results consider homogenized properties and local distributions of stress. For the latter, all six

Table 4: Summary of VD-1 and VD-2

VD-1	
RVE considered	RVE-1 and RVE-2
Void volume fractions	1, 2, 3, 4, 5 %
Subcases per void volume fractions	100
VD-2	
RVE considered	RVE-2
Void volume fractions	1, 2, 3, 4, 5 %
Subcases per void volume fractions	100

strains were applied separately, and, in each case, the strain is 0.2%. The statistical parameters employed are the following [39, 40]: mean value $\bar{x}$, median q_2, standard deviation s, minimum value min, maximum value max, first quartile q_1, third quartile q_3. Such parameters were computed on the maximum values of stress components of a given void distribution and content.

4.2.1 Influence of void distribution on homogenized properties

The first numerical assessment focuses on the homogenized properties. Tables 5 and 6 presents the results regarding VD-1 and both RVE. Table 7 shows the results for RVE-2 and considering VD-2. The results suggest the following:

- As expected, the void content affects the mechanical properties with the degradation that can reach 4%. The standard deviation is very low in all cases.
- The use of a deeper RVE does not affect the mean values; that is, there is no significant influence on the homogenized properties. Likewise, the adoption of different void distributions does not lead to significant modifications of the properties.
- The influence of RVE and void content on the standard deviation is more evident, but, in all cases, s is low.

Table 5: Mean value ($\bar{x}$) and standard deviation (s) of the homogenized properties, RVE-1 and VD-1

		Void content (%)				
		1	2	3	4	5
$\bar{x}$ (GPa)	E_{11}	135.846	135.809	135.771	135.734	135.697
	E_{22}	9.887	9.818	9.747	9.679	9.609
	E_{33}	9.836	9.765	9.695	9.625	9.555
	G_{12}	5.156	5.127	5.098	5.069	5.040
	G_{13}	4.993	4.964	4.935	4.906	4.877
	G_{23}	3.125	3.102	3.080	3.057	3.034
s (MPa)	E_{11}	0.744	1.100	1.056	1.258	1.460
	E_{22}	2.641	3.425	3.480	3.755	4.471
	E_{33}	2.264	2.735	3.388	4.493	3.960
	G_{12}	1.869	2.132	2.508	2.733	3.039
	G_{13}	1.496	1.956	2.502	2.923	2.828
	G_{23}	0.571	0.953	0.887	1.026	1.316

Table 6: Mean value ($\bar{x}$) and standard deviation (s) of the homogenized properties, RVE-2 and VD-1

		Void content (%)				
		1	2	3	4	5
$\bar{x}$ (GPa)	E_{11}	135.846	135.809	135.772	135.734	135.697
	E_{22}	9.887	9.818	9.749	9.679	9.609
	E_{33}	9.836	9.766	9.696	9.625	9.555
	G_{12}	5.156	5.127	5.098	5.069	5.040
	G_{13}	4.993	4.964	4.935	4.906	4.878
	G_{23}	3.125	3.103	3.080	3.057	3.034
s (MPa)	E_{11}	0.508	0.680	0.784	0.850	0.963
	E_{22}	1.470	2.174	2.231	2.910	3.108
	E_{33}	1.307	2.036	2.761	2.405	3.127
	G_{12}	1.064	1.673	1.835	1.979	2.064
	G_{13}	0.969	1.304	1.894	1.790	2.165
	G_{23}	0.456	0.580	0.647	0.790	0.868

Table 7: Mean value ($\bar{x}$) and standard deviation (s) of the homogenized properties, RVE-2 and VD-2

		Void content (%)				
		1	2	3	4	5
$\bar{x}$ (GPa)	E_{11}	135.846	135.809	135.772	135.734	135.697
	E_{22}	9.887	9.818	9.749	9.679	9.610
	E_{33}	9.836	9.766	9.696	9.625	9.555
	G_{12}	5.156	5.127	5.098	5.069	5.040
	G_{13}	4.994	4.964	4.936	4.906	4.877
	G_{23}	3.125	3.103	3.080	3.057	3.034
s (MPa)	E_{11}	0.511	0.682	0.686	0.825	0.919
	E_{22}	1.566	1.955	2.330	2.680	2.527
	E_{33}	1.540	2.047	2.339	2.692	2.794
	G_{12}	1.120	1.448	1.765	1.824	1.921
	G_{13}	1.064	1.194	1.585	1.816	1.970
	G_{23}	0.417	0.573	0.658	0.771	0.936

4.2.2 Influence of void distribution on stress fields

The second numerical assessment concerns the influence of RVE and VD on the stress distributions. Table 8 shows the statistical parameters regarding the maximum values of axial stress found in the RVE-1 having VD-1 and under various axial strains. The first column indicates the applied strain, the second one the stress component, whereas the last one shows the void content. Similarly, Tables 9 and 10 presents the statistical parameters obtained by applying shear strains. The results of RVE-2 with VD-1 are in Tables 11, 12, and 13. Figure 13 shows the box plots of the RVE-1 with VD-1 and applied axial strains. The most relevant stress components are reported. The box plot displays simultaneously several features of the data set [40]. The left side of the box is the first quartile (q_1), and the right side is the third quartile (q_3). The difference $q_3 - q_1$ is the interquartile range (IQR). The vertical line inside the box is the second quartile or median (q_2). The dashed horizontal line on the left of the box connects q_1 to the smallest data point within 1.5 IQR. Similarly, the one on the right side connects q_3 to the largest data point within 1.5 IQR. Data points falling beyond these ranges are indicated explicitly. For example, considering the case of 5% voids and ϵ_{xx} for RVE-1, the highest maximum stress is 106.8 MPa. q_1, q_2 and q_3 are 72.6, 77.6 and 84 MPa, respectively. The lowest minimum of stress is 62.8 MPa. Figures 14, 15, and 16 are the box plots with applied shear strains for RVE-1 and both strains for RVE-2. The results of VD-2 are in Tables 14, 15, and 16, and Figures 17 and 18. Figure 19 shows an example of stress distributions over a cross-section of the RVE. The cross-sections are those in which the peak values were found. The results suggest the following

- There is a general increase of stresses moving from RVE-1 to RVE-2 and VD-1 to VD-2. In other words, by considering deeper RVE and clustering, higher stresses were found.
- By considering the locations of stress peaks, they were found in the proximity of voids and at the interfaces between fibers and matrix.
- The increase of void content leads to higher stresses and wider stress ranges. Several box plots show rightward skewness of the data, i.e., quite high-stress peaks as compared to the mean value.
- As expected, by applying a longitudinal strain (ϵ_{yy}), most of the load is carried by the fibers. The increase of the void content causes a slight increase in the fiber load as it deteriorates the matrix stiffness.

Table 8: Statistical parameters of the axial stresses (MPa) for various void contents (%) with applied ϵ_{xx}, ϵ_{yy}, and ϵ_{zz}, RVE-1 and VD-1

		$\bar{x}$	q_2	s	min	max	q_1	q_3	Voids
ϵ_{xx}	σ_{xx}^{max}	56.670	56.197	4.841	47.949	75.549	53.463	59.128	1
		63.619	62.368	6.083	53.205	83.828	59.979	67.256	2
		67.209	66.043	6.359	57.859	93.672	62.654	69.749	3
		72.385	71.975	6.880	60.132	93.625	67.939	76.037	4
		78.668	77.614	8.927	62.752	106.830	72.615	84.004	5
	σ_{yy}^{max}	37.084	36.600	3.283	30.820	49.030	35.126	39.027	1
		41.574	40.554	4.313	34.638	56.720	38.633	44.150	2
		43.947	43.016	4.106	35.976	60.923	41.084	45.546	3
		47.270	46.986	4.529	38.287	60.974	44.018	49.376	4
		51.387	50.242	6.131	40.111	71.246	47.215	55.293	5
	σ_{zz}^{max}	36.775	36.527	3.384	29.576	48.887	34.566	38.607	1
		41.407	40.373	4.579	34.433	58.128	37.979	44.188	2
		43.690	42.999	4.356	36.284	59.424	40.579	45.822	3
		46.611	46.085	4.604	38.434	60.719	43.152	49.202	4
		50.750	49.705	6.247	39.652	71.785	46.245	54.809	5
ϵ_{yy}	σ_{xx}^{max}	21.365	21.054	1.711	18.488	26.995	20.335	21.940	1
		24.380	23.896	2.536	20.487	33.686	22.556	25.751	2
		26.259	25.687	2.712	21.732	38.296	24.671	26.999	3
		27.632	27.079	2.638	23.758	38.414	25.733	28.771	4
		30.354	29.779	3.658	23.973	45.779	27.550	32.587	5
	σ_{yy}^{max}	456.784	456.729	0.793	455.612	459.420	456.152	457.119	1
		457.711	457.614	1.069	456.125	461.168	456.913	458.224	2
		458.522	458.341	1.130	456.457	462.539	457.818	459.155	3
		459.116	458.877	1.216	456.268	462.540	458.293	459.875	4
		459.767	459.580	1.315	457.277	463.191	458.828	460.451	5
	σ_{zz}^{max}	21.686	21.250	1.772	18.776	26.737	20.321	22.931	1
		25.415	24.498	3.936	20.010	43.822	22.755	26.549	2
		27.733	26.797	4.229	22.349	44.956	24.731	29.240	3
		29.762	28.635	4.343	23.900	44.237	26.767	31.276	4
		31.531	30.300	4.508	25.207	46.899	28.297	33.226	5
ϵ_{zz}	σ_{xx}^{max}	37.967	37.228	3.636	30.741	49.088	35.709	39.420	1
		43.580	41.379	7.155	35.145	80.370	39.059	46.015	2
		47.999	46.647	7.202	35.386	72.759	43.037	50.447	3
		51.617	48.708	8.836	39.474	81.787	45.579	55.250	4
		53.271	51.648	8.195	39.851	79.988	47.618	56.238	5
	σ_{yy}^{max}	38.673	38.031	3.561	32.136	50.242	36.481	40.160	1
		44.237	42.425	7.075	36.116	79.411	39.652	46.604	2
		48.770	47.737	7.144	37.803	75.340	43.465	52.086	3
		52.709	50.127	8.716	41.658	79.996	47.246	55.247	4
		54.410	52.991	8.124	41.642	83.652	48.430	58.174	5
	σ_{zz}^{max}	59.310	58.232	5.392	50.047	76.481	56.026	61.267	1
		67.781	65.093	10.457	54.467	118.228	60.751	71.349	2
		74.608	72.414	10.733	60.051	115.875	66.339	79.398	3
		80.906	77.128	13.076	61.675	122.699	73.160	84.118	4
		83.825	81.378	11.946	63.852	129.370	75.342	89.852	5

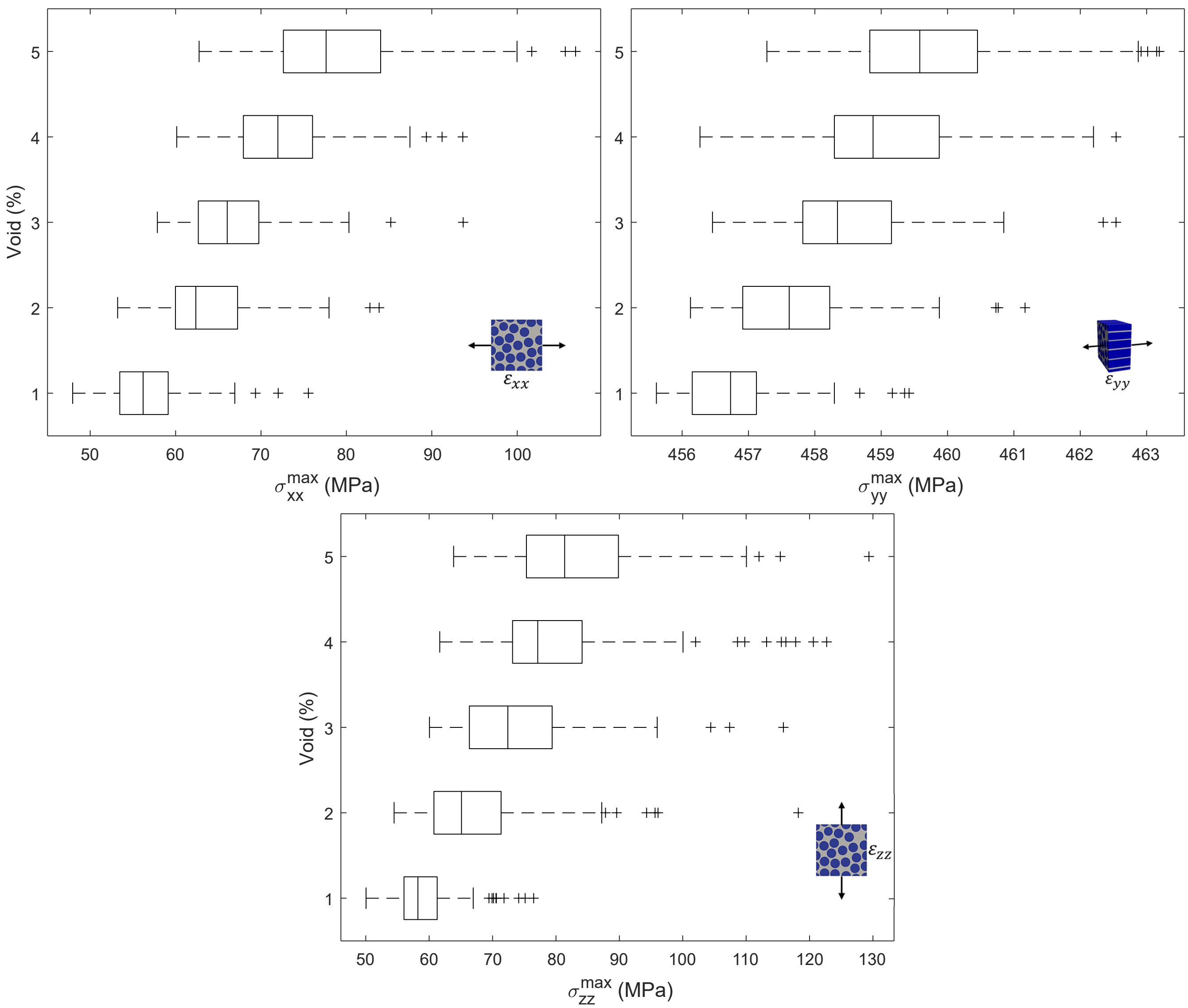

Figure 13: Box plots of axial stresses with applied axial strains, RVE-1 and VD-1

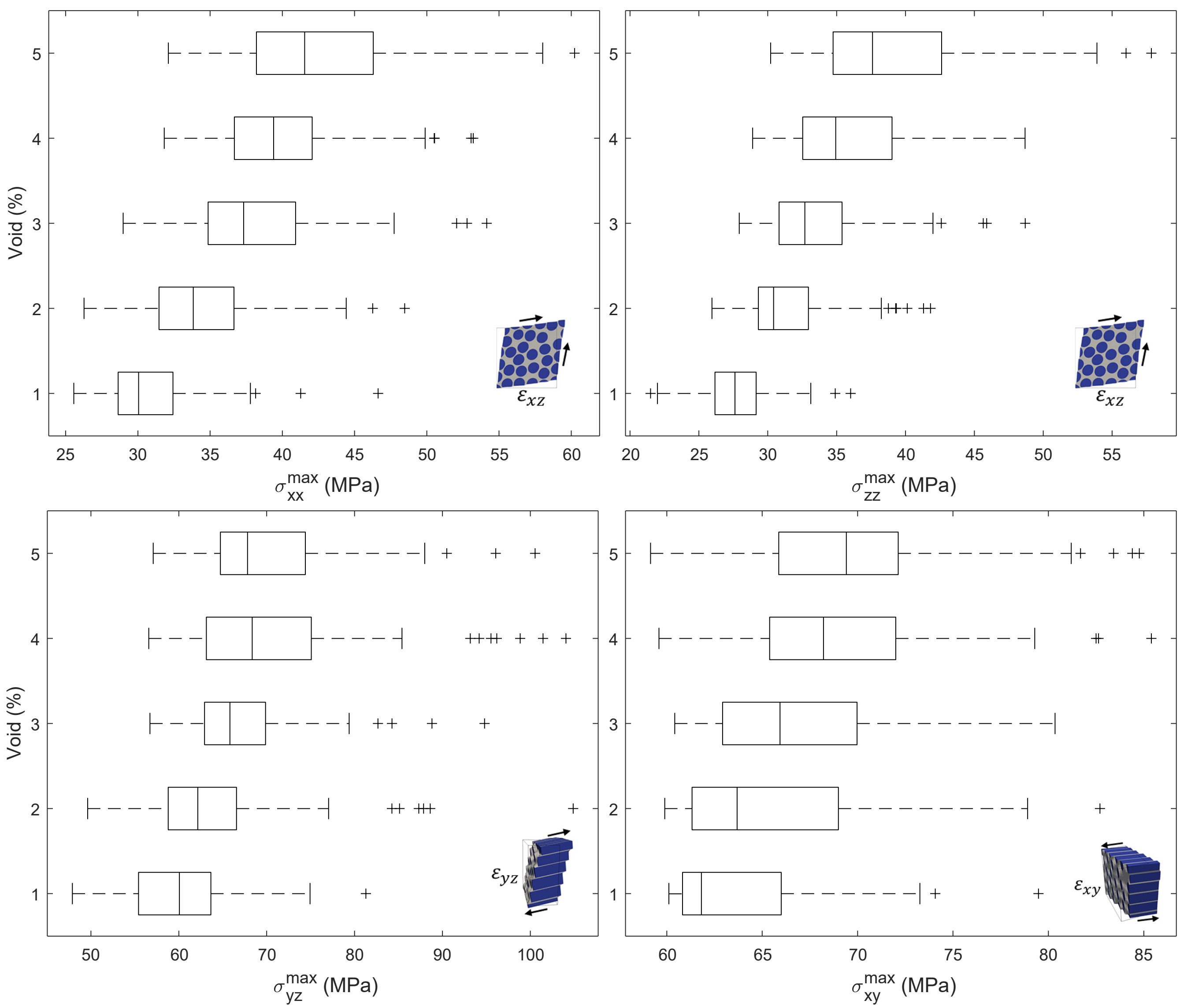

Figure 14: Box plots of stress components with applied shear strains, RVE-1 and VD-1

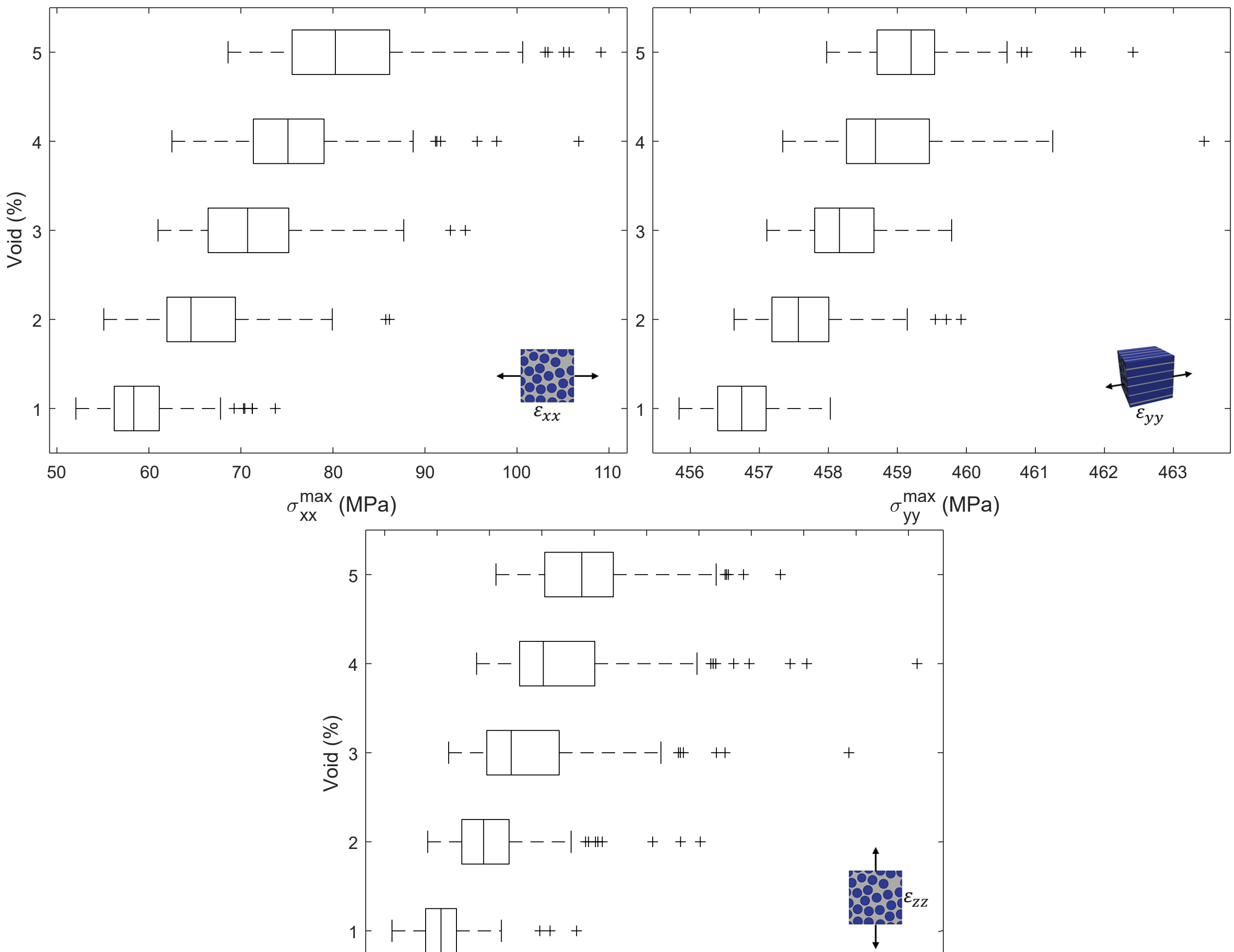

Figure 15: Box plots of axial stresses with applied axial strains, RVE-2 and VD-1

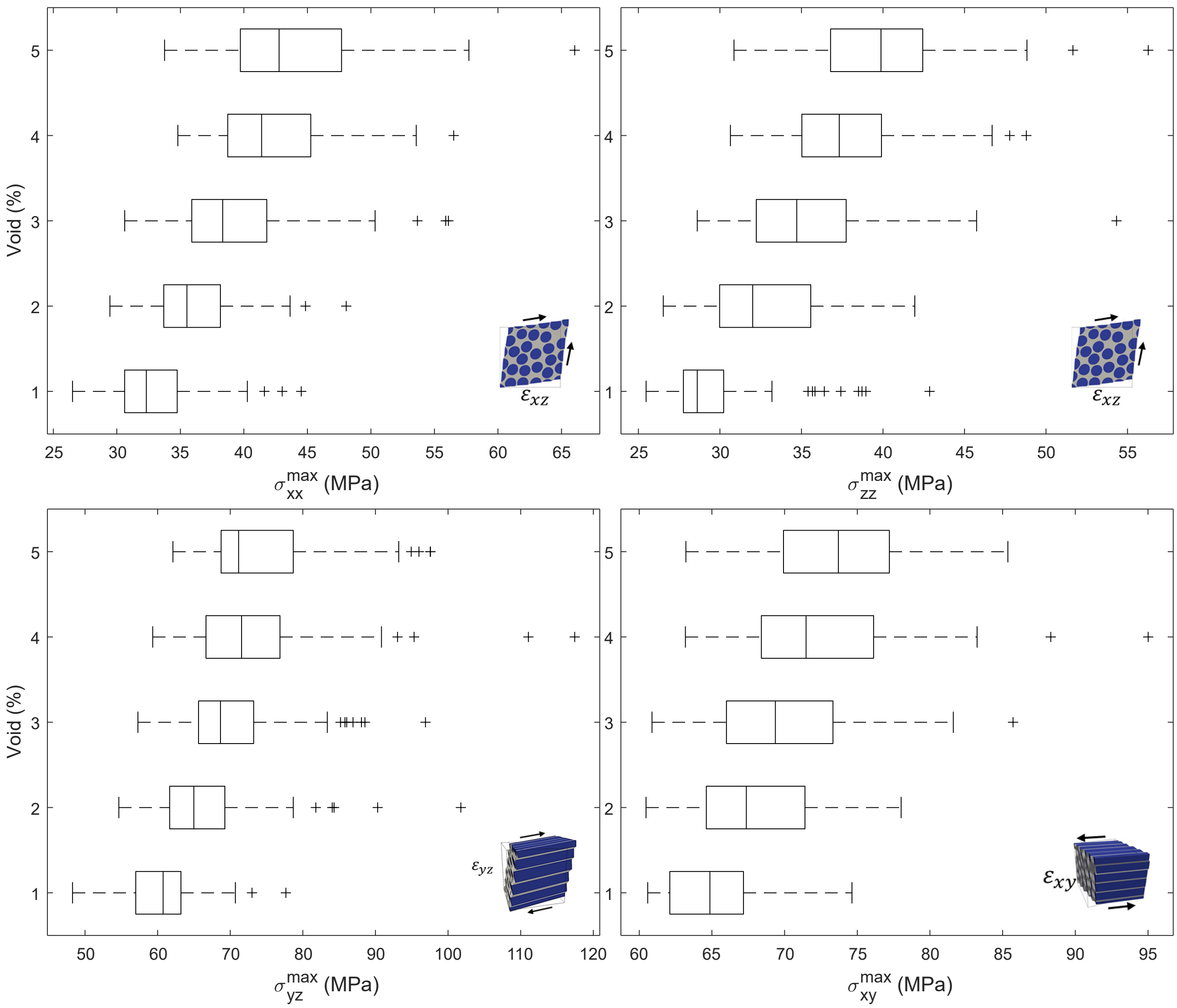

Figure 16: Box plots of stress components with applied shear strains, RVE-2 and VD-1

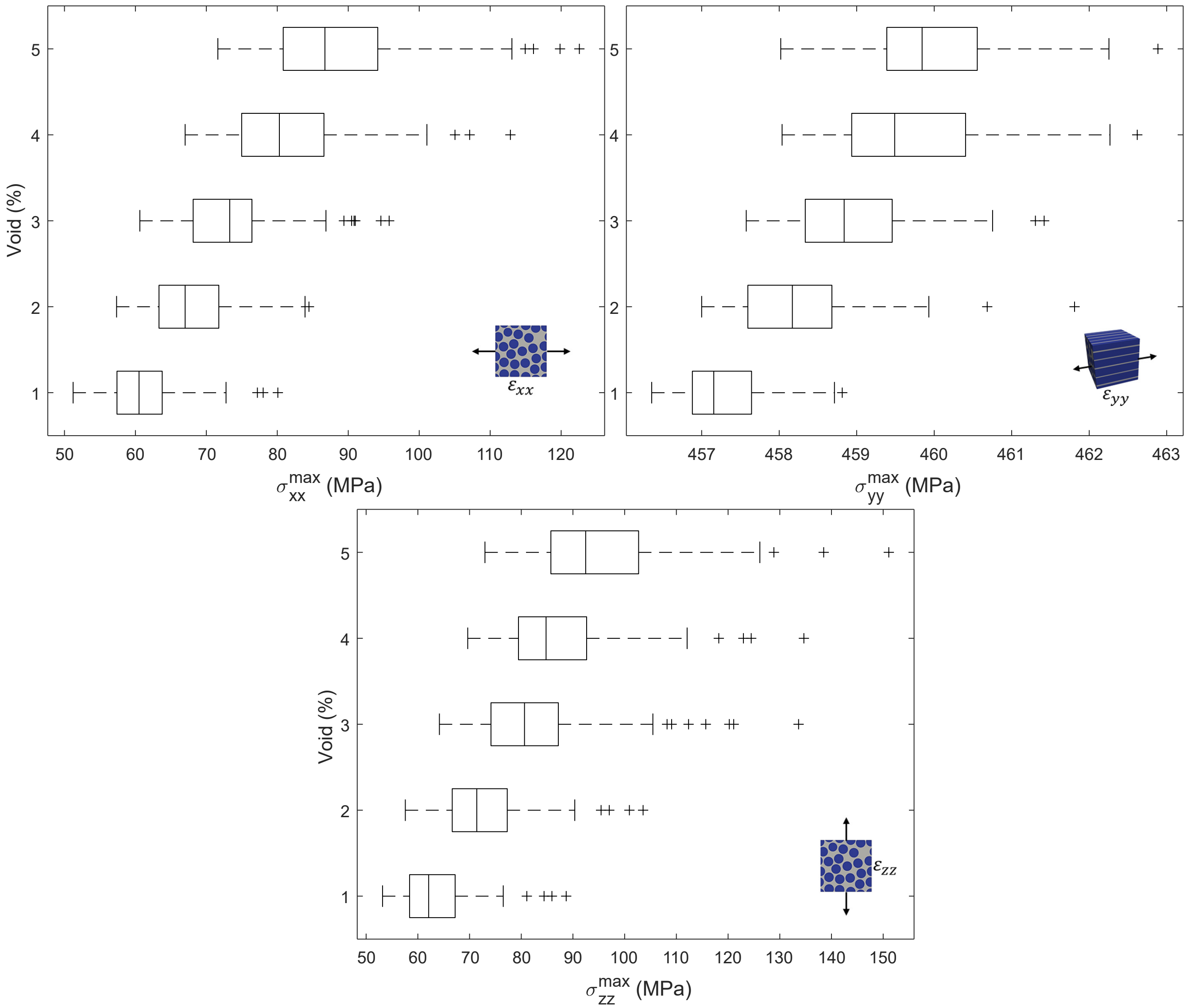

Figure 17: Box plots of stress components with applied axial strains, RVE-2 and VD-2

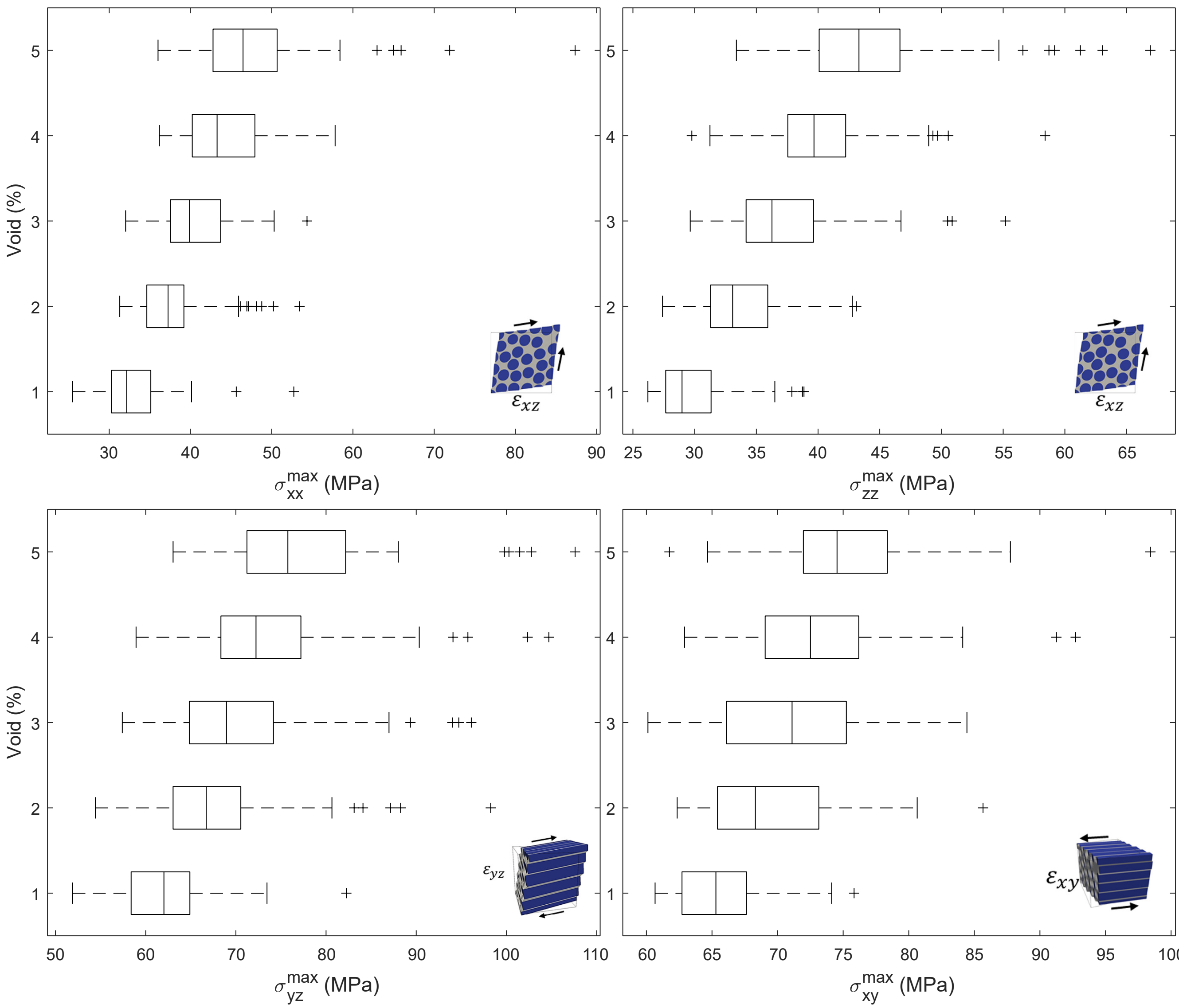

Figure 18: Box plots of stress components with applied shear strains, RVE-2 and VD-2

Table 9: Statistical parameters of stresses (MPa) for various void contents (%) with applied ϵ_{xz}, RVE-1 and VD-1

	$\bar{x}$	q_2	s	min	max	q_1	q_3	Voids
σ_{xx}^{max}	30.805	30.050	3.415	25.565	46.629	28.635	32.427	1
	34.537	33.835	4.170	26.272	48.472	31.461	36.653	2
	38.093	37.324	5.138	28.982	54.148	34.863	40.916	3
	39.908	39.397	4.557	31.828	53.213	36.679	42.068	4
	42.705	41.544	5.721	32.111	60.232	38.208	46.298	5
σ_{yy}^{max}	22.234	22.371	2.278	18.175	31.514	20.228	23.627	1
	25.130	24.513	2.889	20.277	35.152	23.448	26.018	2
	27.535	27.161	3.586	21.789	38.993	25.277	29.220	3
	29.044	28.498	3.446	22.878	39.533	26.713	30.997	4
	31.553	30.680	4.652	23.472	46.079	28.268	34.002	5
σ_{zz}^{max}	27.696	27.621	2.648	21.492	36.014	26.165	29.158	1
	31.258	30.426	3.326	25.948	41.815	29.317	32.955	2
	33.543	32.692	4.062	27.929	48.693	30.819	35.393	3
	35.801	34.934	4.262	28.906	48.680	32.539	39.023	4
	39.403	37.604	6.398	30.211	57.848	34.744	42.619	5
σ_{xz}^{max}	23.332	22.787	1.310	22.086	30.339	22.477	23.749	1
	25.533	24.852	2.831	22.225	35.063	23.441	26.449	2
	25.883	25.173	2.420	22.469	33.916	24.117	27.093	3
	27.396	26.760	3.137	23.077	38.418	24.836	28.798	4
	28.870	28.518	3.390	23.295	39.246	26.260	31.173	5

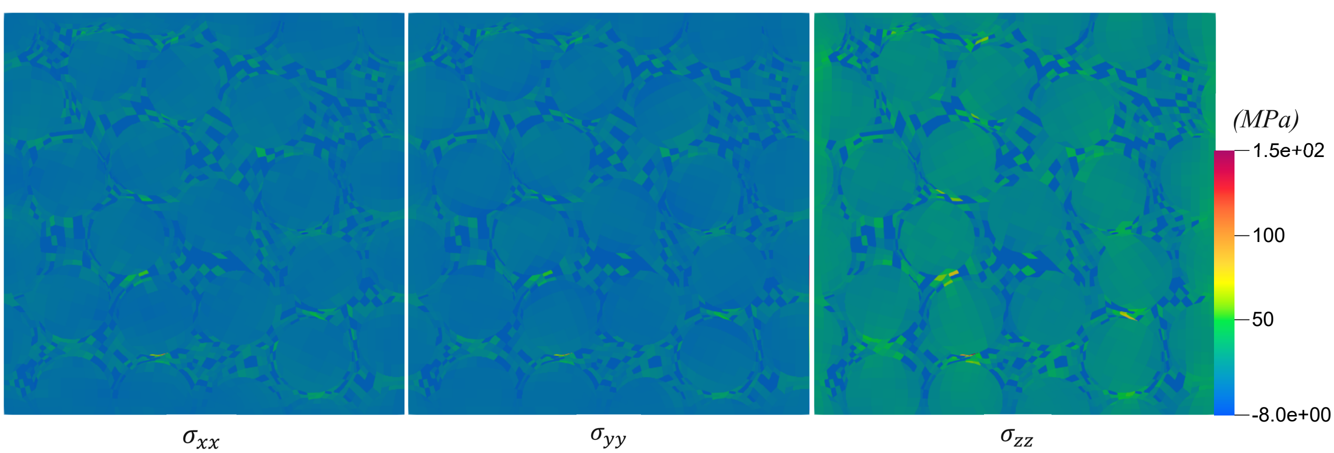

Figure 19: Cross-section distributions of stresses in which peak values were found, void content 5%, applied ϵ_{zz}, RVE-2 and VD-2

Table 10: Statistical parameters of stresses (MPa) for various void contents (%) with applied ϵ_{xy} and ϵ_{yz}, RVE-1 and VD-1

		$\bar{x}$	q_2	s	min	max	q_1	q_3	Voids
ϵ_{xy}	σ_{yy}^{max}	21.784	21.118	6.195	11.855	45.525	17.085	24.162	1
		30.693	30.031	6.467	19.520	49.347	25.708	34.987	2
		36.921	35.692	6.793	25.062	56.996	32.120	40.700	3
		43.298	40.832	8.730	30.106	70.883	36.463	47.364	4
		49.871	48.275	8.511	34.598	71.430	43.836	53.535	5
	σ_{xy}^{max}	63.376	61.813	3.844	60.111	79.480	60.825	65.998	1
		65.501	63.685	4.896	59.892	82.703	61.322	68.995	2
		67.107	65.933	4.863	60.415	80.350	62.924	69.972	3
		68.973	68.214	5.266	59.588	85.396	65.391	71.999	4
		69.565	69.412	5.191	59.149	84.766	65.866	72.130	5
	σ_{yz}^{max}	21.530	21.230	1.633	19.450	26.227	20.159	22.372	1
		22.833	22.759	1.848	19.665	31.435	21.480	23.895	2
		23.954	23.750	2.069	19.957	28.814	22.417	25.223	3
		24.520	24.335	2.064	19.877	31.635	23.181	25.785	4
		25.685	25.163	2.470	21.635	33.578	23.880	27.293	5
ϵ_{yz}	σ_{yy}^{max}	19.791	19.022	5.395	12.292	41.777	15.880	21.845	1
		27.668	27.137	5.674	16.378	48.906	23.592	31.313	2
		35.047	33.804	6.981	22.704	59.602	30.311	38.709	3
		41.319	40.862	6.482	29.860	62.146	37.005	44.087	4
		47.408	45.947	7.481	33.746	67.329	41.824	52.463	5
	σ_{xy}^{max}	24.920	23.979	2.071	23.089	33.275	23.556	25.799	1
		26.323	25.987	2.530	23.041	34.810	23.989	27.674	2
		28.028	27.353	3.131	23.126	36.069	25.723	29.877	3
		28.667	28.144	3.436	23.301	40.553	26.521	30.229	4
		30.703	30.166	3.352	24.011	39.322	28.148	32.857	5
	σ_{yz}^{max}	59.737	60.069	6.250	47.890	81.287	55.421	63.651	1
		63.582	62.157	8.476	49.629	104.874	58.792	66.568	2
		67.037	65.812	6.561	56.721	94.796	62.925	69.869	3
		70.015	68.356	10.103	56.585	104.051	63.138	75.074	4
		70.348	67.821	7.816	57.085	100.543	64.730	74.396	5

Table 11: Statistical parameters of stresses (MPa) for various void contents (%) with applied ϵ_{xx}, ϵ_{yy}, ϵ_{zz}, RVE-2 and VD-1

		$\bar{x}$	q_2	s	min	max	q_1	q_3	Voids
ϵ_{xx}	σ_{xx}^{max}	59.086	58.353	4.574	52.065	73.738	56.227	61.126	1
		65.992	64.571	5.913	55.098	86.136	61.962	69.396	2
		71.621	70.726	6.690	60.990	94.387	66.437	75.202	3
		76.181	75.115	7.391	62.506	106.706	71.354	79.036	4
		82.136	80.263	9.221	68.600	109.120	75.567	86.160	5
	σ_{yy}^{max}	38.845	38.192	3.154	34.079	47.219	36.894	40.171	1
		43.033	42.273	4.078	35.090	56.107	40.010	45.508	2
		46.653	46.357	4.131	39.283	58.505	43.468	48.616	3
		49.684	48.804	4.974	41.135	69.396	46.422	51.477	4
		53.363	51.473	6.053	44.754	71.528	48.977	56.216	5
	σ_{zz}^{max}	38.624	37.915	3.311	33.174	47.847	36.495	40.463	1
		42.904	42.201	4.406	34.439	58.216	39.591	45.357	2
		45.916	45.034	3.886	39.075	58.814	43.318	47.910	3
		48.920	48.363	5.289	40.645	66.979	45.315	50.722	4
		52.360	50.680	6.238	43.006	71.232	48.325	54.997	5
ϵ_{yy}	σ_{xx}^{max}	22.057	21.686	1.562	19.473	27.567	20.831	23.033	1
		25.374	24.761	2.428	21.839	33.653	23.752	26.403	2
		27.675	27.257	2.686	23.220	35.950	25.538	29.087	3
		29.362	28.967	2.985	23.974	42.264	27.345	30.883	4
		31.547	30.340	4.260	26.726	51.214	28.757	32.494	5
	σ_{yy}^{max}	456.799	456.744	0.509	455.837	458.028	456.397	457.098	1
		457.665	457.565	0.672	456.633	459.922	457.182	458.006	2
		458.286	458.161	0.668	457.109	459.787	457.801	458.660	3
		458.955	458.682	0.990	457.338	463.445	458.261	459.463	4
		459.261	459.198	0.788	457.975	462.414	458.705	459.539	5
	σ_{zz}^{max}	22.625	22.400	1.871	19.932	30.225	21.333	23.684	1
		26.581	25.273	3.917	21.703	46.122	24.399	27.565	2
		29.201	28.018	4.304	23.847	48.341	26.482	30.231	3
		31.484	29.935	5.305	25.590	55.035	27.900	32.588	4
		33.069	32.105	4.112	26.405	45.406	29.887	35.026	5
ϵ_{zz}	σ_{xx}^{max}	39.330	38.785	3.711	32.825	55.203	36.998	41.021	1
		45.588	43.364	6.964	36.173	75.418	41.508	47.042	2
		49.808	47.958	8.707	38.861	88.736	43.932	53.097	3
		54.795	51.412	10.315	41.795	104.810	47.898	59.691	4
		57.269	54.665	8.658	44.970	83.411	51.214	61.796	5
	σ_{yy}^{max}	40.086	39.590	3.678	33.460	56.653	37.981	41.792	1
		46.393	44.784	6.818	36.278	74.171	42.230	48.258	2
		50.643	48.531	8.742	39.696	91.030	44.589	54.456	3
		55.528	51.451	10.114	42.924	102.507	49.040	59.394	4
		58.244	56.213	8.326	46.350	83.372	51.958	61.345	5
	σ_{zz}^{max}	61.490	60.748	5.603	51.402	86.630	57.813	63.710	1
		71.066	68.876	9.865	58.211	110.253	64.723	73.759	2
		77.824	74.160	13.015	62.214	138.632	69.479	83.314	3
		85.117	80.287	14.718	67.544	151.642	75.752	90.106	4
		89.242	87.643	12.010	71.256	125.561	80.559	93.652	5

Table 12: Statistical parameters of stresses (MPa) for various void contents (%) with applied ϵ_{xz}, RVE-2 and VD-1

	$\bar{x}$	q_2	s	min	max	q_1	q_3	Voids
	32.767	32.319	3.446	26.510	44.510	30.611	34.751	1
	36.017	35.512	3.425	29.454	48.059	33.690	38.151	2
σ_{xx}^{max}	39.285	38.334	4.576	30.620	56.095	35.895	41.802	3
	42.610	41.396	4.990	34.802	56.516	38.725	45.264	4
	44.116	42.772	5.809	33.754	66.041	39.720	47.688	5
	23.626	23.185	2.302	20.092	31.829	22.337	24.424	1
	26.079	26.024	2.512	21.805	35.437	24.336	27.393	2
σ_{yy}^{max}	28.590	28.122	3.216	23.405	43.579	26.226	30.115	3
	30.838	30.872	3.278	25.150	39.111	27.985	33.019	4
	32.180	31.488	3.944	25.201	46.000	29.641	34.641	5
	29.516	28.611	3.092	25.473	42.860	27.759	30.228	1
	32.688	32.010	3.532	26.525	41.951	29.982	35.574	2
σ_{zz}^{max}	35.315	34.712	4.251	28.611	54.328	32.231	37.741	3
	37.839	37.318	4.015	30.645	48.793	35.024	39.910	4
	39.838	39.881	4.213	30.862	56.272	36.787	42.442	5
	23.951	23.738	1.447	22.199	29.425	22.781	24.715	1
	26.216	25.583	2.520	22.534	36.084	24.593	27.471	2
σ_{xz}^{max}	27.619	27.162	2.810	22.868	39.971	25.700	29.040	3
	28.650	28.126	2.617	24.548	41.136	26.927	29.869	4
	30.031	29.514	3.651	25.055	42.677	27.142	32.170	5

- σ_{xx} and σ_{zz} is the stress component with the highest values in the matrix. In some cases, the increase of this component reached three times the value of the pristine RVE.

Further analyses can make use of the probability density function [39] as shown in Figs. 20 and 21. The aim is to show the major differences in the results stemming from the three modeling approaches, namely, RVE-1 and VD-1, RVE-2 and VD-1, and RVE-2 and VD-2. As stated above, there is an increase in both the mean and peak values as deeper RVE and clustering are considered. By moving from RVE-1/VD-1 to RVE-2/VD-2, the mean values increased by some 10%.

5 Conclusions

The present work has investigated the influence of matrix voids on the prediction of the homogenized properties and stress fields in RVE for fiber-reinforced polymer composites. The assessments are numerical and based on a numerically efficient FE framework and refined 1D structural models from CUF. The RVE models have randomly distributed fibers and voids within the matrix. All three constituents are modeled via a component-wise approach via Lagrange polynomials defining the displacement field and the geometry. The use of 1D models avoids the aspect ratio constraints of 3D FE and leads to significantly

Table 13: Statistical parameters of stresses (MPa) for various void contents (%) with applied ϵ_{yz} and ϵ_{xy}, RVE-2 and VD-1

		$\bar{x}$	q_2	s	min	max	q_1	q_3	Voids
ϵ_{yz}	σ_{yy}^{max}	20.020	19.301	4.532	11.050	35.085	16.953	22.898	1
		27.768	26.507	6.810	17.752	53.593	22.986	29.985	2
		32.251	30.610	5.944	22.022	48.272	27.419	35.547	3
		38.163	36.618	8.120	23.685	58.861	31.776	43.498	4
		41.886	40.531	7.193	29.472	60.791	35.895	47.705	5
	σ_{xy}^{max}	25.900	25.516	2.101	23.338	33.271	23.953	27.415	1
		27.200	27.059	2.433	23.652	35.062	25.201	28.757	2
		29.144	28.554	2.968	23.558	39.388	27.234	31.167	3
		30.633	29.866	3.777	24.850	42.728	27.808	32.637	4
		31.346	30.510	3.869	25.140	45.029	28.566	33.845	5
	σ_{yz}^{max}	60.572	60.762	4.968	48.284	77.659	56.989	63.214	1
		66.553	64.988	7.414	54.657	101.766	61.653	69.257	2
		70.233	68.658	7.139	57.289	96.886	65.634	73.226	3
		73.706	71.556	9.671	59.329	117.436	66.662	76.852	4
		73.963	71.153	8.176	62.108	97.577	68.744	78.685	5
ϵ_{xy}	σ_{yy}^{max}	22.565	22.174	5.419	12.646	46.350	18.364	25.469	1
		30.965	29.366	7.871	15.009	66.575	26.259	33.711	2
		33.777	31.783	7.372	21.799	56.058	28.692	36.546	3
		39.585	38.555	8.006	25.038	65.015	33.669	43.868	4
		44.343	42.294	9.157	29.837	74.184	37.520	49.710	5
	σ_{xy}^{max}	65.118	64.859	3.490	60.580	74.632	62.103	67.171	1
		67.810	67.368	4.508	60.467	78.017	64.616	71.403	2
		69.975	69.362	4.958	60.876	85.716	65.998	73.325	3
		72.375	71.477	5.551	63.173	95.013	68.403	76.123	4
		73.706	73.696	5.093	63.207	85.359	69.924	77.209	5
	σ_{yz}^{max}	22.067	21.734	1.468	19.713	25.920	20.996	22.934	1
		23.150	22.732	1.681	19.762	27.572	21.943	24.216	2
		24.595	24.502	1.937	21.794	34.707	23.237	25.341	3
		25.302	25.016	1.844	21.704	31.895	23.959	26.641	4
		26.028	25.592	2.163	22.031	33.482	24.404	27.289	5

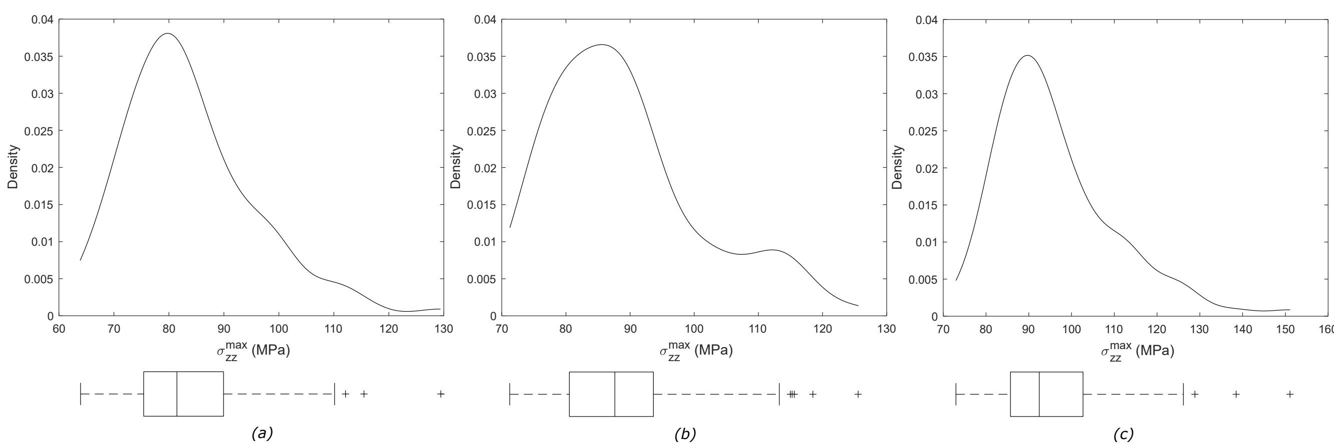

Figure 20: Fitting of the probability density function of σ_{zz}^{max} with applied ϵ_{zz} (a) RVE-1 and VD-1, (b) RVE-2 and VD-1, (b) RVE-2 and VD-2, void content 5%

Table 14: Statistical parameters of the axial stresses (MPa) for various void contents (%) with applied ϵ_{xx}, ϵ_{yy}, ϵ_{zz}, RVE-2 and VD-2

		$\bar{x}$	q_2	s	min	max	q_1	q_3	Voids
ϵ_{xx}	σ_{xx}^{max}	61.184	60.513	5.420	51.224	80.075	57.401	63.775	1
		68.120	67.009	6.479	57.352	84.459	63.328	71.757	2
		73.616	73.292	7.045	60.621	95.766	68.139	76.427	3
		81.647	80.292	8.969	67.006	112.855	74.983	86.571	4
		88.384	86.704	10.851	71.621	122.568	80.835	94.156	5
	σ_{yy}^{max}	40.114	39.585	3.715	33.903	52.691	37.195	42.301	1
		44.505	43.602	4.582	36.722	55.507	40.712	47.476	2
		48.049	46.903	4.703	39.253	60.303	44.565	50.210	3
		53.014	52.126	5.967	44.620	75.771	48.688	56.000	4
		57.265	56.281	7.259	45.180	82.883	52.087	61.074	5
	σ_{zz}^{max}	39.811	38.870	3.900	33.616	52.128	36.866	42.412	1
		44.218	43.421	4.736	35.187	55.609	40.608	46.922	2
		47.793	47.275	4.681	39.196	59.951	44.829	50.088	3
		52.135	50.979	6.274	42.419	79.755	47.546	55.520	4
		56.144	54.872	7.290	41.707	85.881	51.257	59.882	5
ϵ_{yy}	σ_{xx}^{max}	22.866	22.151	2.369	19.637	31.509	21.278	24.125	1
		26.168	25.364	2.567	22.763	34.504	24.079	27.980	2
		28.521	28.007	2.817	23.172	40.033	26.839	29.830	3
		31.286	30.456	3.531	26.334	45.258	28.994	32.568	4
		33.911	33.667	4.004	27.330	46.940	30.669	36.192	5
	σ_{yy}^{max}	457.284	457.156	0.552	456.355	458.813	456.880	457.644	1
		458.239	458.170	0.819	457.000	461.811	457.595	458.680	2
		458.946	458.838	0.793	457.575	461.419	458.336	459.458	3
		459.707	459.490	0.976	458.037	462.620	458.936	460.405	4
		459.983	459.844	0.866	458.020	462.887	459.389	460.556	5
	σ_{zz}^{max}	23.566	22.745	2.524	19.554	31.632	21.862	24.934	1
		26.963	26.282	3.284	21.994	38.557	24.740	28.313	2
		30.692	29.707	4.496	24.935	53.239	27.897	32.357	3
		32.340	31.371	4.368	26.345	55.498	29.557	34.407	4
		35.936	34.555	4.906	28.757	52.841	32.105	38.669	5
ϵ_{zz}	σ_{xx}^{max}	40.884	39.986	4.289	33.392	57.787	37.971	43.399	1
		46.842	45.322	6.268	35.751	69.818	42.370	49.646	2
		52.476	51.505	8.343	40.776	89.037	46.746	55.205	3
		55.604	53.630	7.955	44.153	88.789	49.953	58.041	4
		60.714	58.703	9.607	48.107	103.831	54.355	65.274	5
	σ_{yy}^{max}	41.576	40.548	4.476	34.441	57.409	38.447	44.151	1
		47.688	46.730	6.036	37.894	69.273	43.320	50.476	2
		53.528	52.091	8.501	41.823	89.030	47.383	56.144	3
		56.632	54.894	7.921	44.355	89.260	51.292	59.340	4
		62.257	59.939	9.384	47.014	101.843	56.464	66.879	5
	σ_{zz}^{max}	63.501	62.090	7.024	53.176	88.684	58.399	67.208	1
		73.075	71.401	8.955	57.582	103.572	66.655	77.292	2
		82.106	80.633	12.928	64.174	133.630	74.139	87.171	3
		87.218	84.795	11.703	69.644	134.656	79.457	92.648	4
		96.180	92.460	14.073	72.974	151.082	85.732	102.695	5

Table 15: Statistical parameters of the stresses (MPa) for various void contents (%) with applied ϵ_{xz}, RVE-2 and VD-2

	$\bar{x}$	q_2	s	min	max	q_1	q_3	Voids
	32.989	32.163	4.044	25.498	52.723	30.281	35.119	1
	37.825	37.247	4.337	31.297	53.423	34.628	39.197	2
σ_{xx}^{max}	40.695	39.884	4.293	32.023	54.350	37.516	43.715	3
	44.599	43.274	5.376	36.180	57.803	40.217	47.929	4
	47.680	46.473	7.485	36.011	87.341	42.779	50.664	5
	23.970	23.514	2.522	20.285	35.145	22.029	25.709	1
	27.385	26.824	2.984	22.268	38.468	25.163	29.026	2
σ_{yy}^{max}	29.982	29.079	3.444	22.793	41.750	27.830	31.888	3
	32.563	31.732	3.941	26.255	45.894	29.673	35.459	4
	35.136	34.596	5.267	26.979	59.975	31.538	37.009	5
	29.750	28.976	2.766	26.211	38.862	27.658	31.333	1
	33.682	33.081	3.497	27.400	43.096	31.294	35.923	2
σ_{zz}^{max}	37.313	36.264	4.594	29.645	55.192	34.171	39.632	3
	40.226	39.670	4.597	29.768	58.403	37.550	42.241	4
	44.324	43.313	6.283	33.381	66.927	40.089	46.637	5
	24.560	24.170	1.895	22.350	34.621	23.125	25.373	1
	26.646	26.128	2.818	22.206	35.983	24.560	28.000	2
σ_{xz}^{max}	27.902	27.354	2.887	23.337	41.013	25.770	29.446	3
	29.453	29.013	3.479	24.420	43.170	26.818	31.159	4
	30.902	30.032	3.095	26.062	42.359	28.670	32.773	5

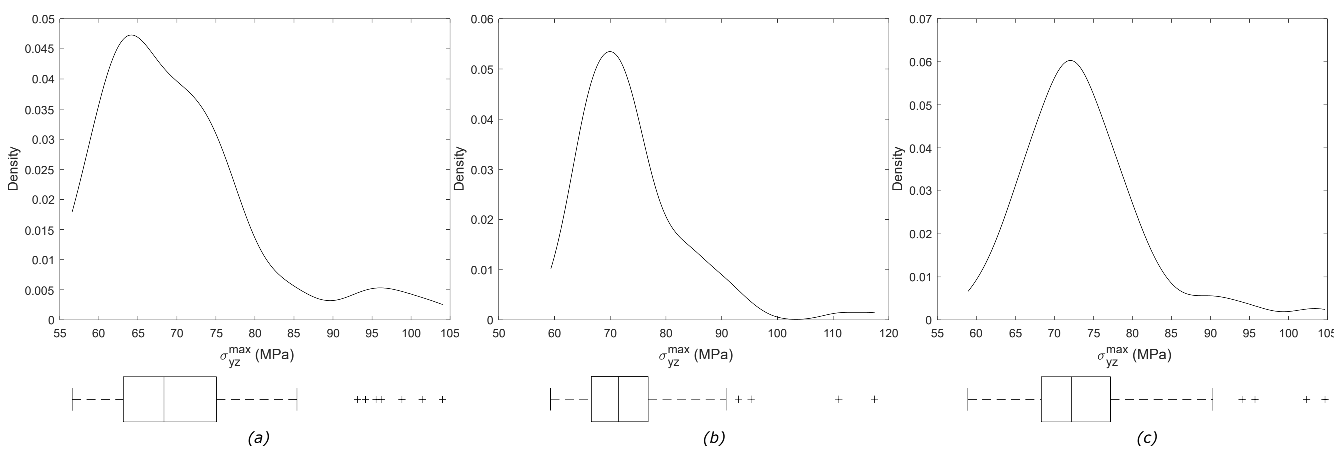

Figure 21: Fitting of the probability density function of σ_{yz}^{max} with applied ϵ_{yz} (a) RVE-1 and VD-1, (b) RVE-2 and VD-1, (b) RVE-2 and VD-2, void content 4%

Table 16: Statistical parameters of the stresses (MPa) for various void contents (%) with applied ϵ_{yz} and ϵ_{xy}, RVE-2 and VD-2

		$\bar{x}$	q_2	s	min	max	q_1	q_3	Voids
ϵ_{yz}	σ_{yy}^{max}	20.290	19.264	5.407	13.098	52.881	16.789	22.535	1
		31.790	31.594	6.446	21.305	56.715	26.491	34.959	2
		40.235	37.751	8.673	27.987	77.049	34.250	42.887	3
		46.519	45.106	7.191	35.307	70.625	41.917	51.084	4
		57.071	56.090	9.011	40.612	82.125	50.009	61.905	5
	σ_{xy}^{max}	25.724	25.044	2.482	23.377	38.514	24.045	26.752	1
		28.199	27.628	2.987	23.464	38.133	26.143	29.557	2
		29.629	29.094	3.231	24.094	40.065	27.266	31.219	3
		31.108	30.273	4.038	24.273	46.375	28.401	33.198	4
		32.239	31.666	4.052	25.462	45.885	29.247	34.163	5
	σ_{yz}^{max}	61.989	62.027	4.920	51.904	82.254	58.386	64.902	1
		67.716	66.712	7.379	54.425	98.255	63.042	70.546	2
		70.507	68.962	7.909	57.407	96.102	64.842	74.168	3
		73.761	72.232	8.135	58.936	104.704	68.343	77.213	4
		77.246	75.763	8.513	63.038	107.611	71.231	82.170	5
ϵ_{xy}	σ_{yy}^{max}	23.606	22.164	6.074	14.351	47.181	19.767	26.322	1
		33.531	32.056	8.677	20.891	74.465	27.439	36.996	2
		42.219	39.942	8.821	26.222	66.975	36.359	46.840	3
		48.904	47.841	7.635	33.686	71.438	43.108	54.139	4
		58.139	55.929	9.302	41.535	92.147	51.706	63.112	5
	σ_{xy}^{max}	65.690	65.300	3.661	60.662	75.835	62.713	67.627	1
		69.364	68.307	4.653	62.345	85.661	65.422	73.146	2
		71.130	71.107	5.694	60.118	84.438	66.109	75.247	3
		72.958	72.508	5.534	62.908	92.724	69.058	76.192	4
		75.239	74.535	5.912	61.754	98.422	71.969	78.361	5
	σ_{yz}^{max}	22.257	21.935	1.702	19.992	27.488	20.958	22.779	1
		23.764	23.419	2.172	20.403	33.136	22.158	24.645	2
		24.815	24.466	2.189	21.597	33.206	23.023	26.072	3
		26.086	25.630	2.174	21.772	32.160	24.626	27.107	4
		27.191	26.770	2.646	22.004	39.498	25.503	28.379	5

lower computational costs. The present framework can deal with various sets of void distributions to investigate the influence of void content and morphology. Such analyses considered multiple scenarios and statistical metrics. The RVE is 3D, and the influence of its depth is another assessed parameter. The most significant findings are the following:

- As well-known, the influence of void distributions and RVE dimensions on the homogenized properties is low. The void content is the fundamental parameter to consider, independently of the void arrangement.

- The void arrangement influences the stress fields. The clustering of voids leads to higher stress mean values and peaks, and broader ranges of stress.

- Likewise, deeper RVE leads to higher stress values. The combined effect - deeper RVE and clustering - may lead to some 10% increments in the mean values of stress.

- All six stress components are affected with particularly significant variations in cross-sectional axial components.

The future extensions should consider the nonlinear analysis to investigate the influence of voids on failure. Furthermore, the modeling of more complex RVE architectures and the multiscale analysis are of interest.

Acknowledgements

This work is supported by the project ICONIC (Improving the Crashworthiness of Composite Transportation Structures), funded by the European Union Horizon 2020 Research and Innovation program under the Marie Skłodowska-Curie Grant agreement No. 721256.

References

[1] E.J. Barbero. *Multifunctional Composites*. Number v. 1 in Multifunctional Composites Series. CreateSpace Independent Publishing Platform, 2015.

[2] R. Talreja and C.V. Singh. *Damage and Failure of Composite Materials*. Cambridge University Press, 2012.

[3] J. Aboudi, S.M. Arnold, and B.A. Bednarcyk. *Micromechanics of Composite Materials: A Generalized Multiscale Analysis Approach*. Elsevier Science, 2013.

[4] D. Gay. *Composite Materials: Design and Applications, Third Edition*. CRC Press, 2014.

[5] R. Talreja and J. Varna. *Modeling Damage, Fatigue and Failure of Composite Materials*. Woodhead Publishing Series in Composites Science and Engineering. Elsevier Science, 2015.

[6] E.K. Gamstedt and B.A. Sjögren. Micromechanisms in tension-compression fatigue of composite laminates containing transverse plies. *Composites Science and Technology*, 59(2):167–178, 1999.

[7] M. Hinton, P.D. Soden, and A.S. Kaddour. *Failure Criteria in Fibre Reinforced Polymer Composites: The World-Wide Failure Exercise*. Elsevier Science, 2004.

[8] M. Mehdikhani, L. Gorbatikh, I. Verpoest, and S. V. Lomov. Voids in fiber-reinforced polymer composites: A review on their formation, characteristics, and effects on mechanical performance. *Journal of Composite Materials*, 53(12):1579–1669, 2019.

[9] C.T. Sun and R.S. Vaidya. Prediction of composite properties from a representative volume element. *Composites Science and Technology*, 56:171–179, 02 1996.

[10] S. Li and E. Sitnikova. *Representative Volume Elements and Unit Cells: Concepts, Theory, Applications and Implementation*. Woodhead Publishing Series in Composites Science and Engineering. Elsevier Science, 2019.

[11] C. Gonzalez and J. Llorca. Mechanical behavior of unidirectional fiber-reinforced polymers under transverse compression: Microscopic mechanisms and modeling. *Composites Science and Technology*, 67:2795–2806, 10 2007.

[12] J. Chevalier, P. Camanho, F. Lani, and T. Pardoen. Multi-scale characterization and modelling of the transverse compression response of unidirectional carbon fiber reinforced epoxy. *Composite Structures*, 209, 10 2018.

[13] T. Hobbiebrunken, M. Hojo, B. Fiedler, M. Tanaka, O. Shojiro, and S. Karl. Thermomechanical analysis of micromechanical formation of residual stresses and initial matrix failure in cfrp. *JSME International Journal Series A*, 47, 07 2004.

[14] L. Yang, X. Liu, Z. Wu, and R. Wang. Effects of triangle-shape fiber on the transverse mechanical properties of unidirectional carbon fiber reinforced plastics. *Composite Structures*, 152, 05 2016.

[15] F. Naya, C. González, C.s Lopes, S. Veen, and F. Pons. Computational micromechanics of the transverse and shear behavior of unidirectional fiber reinforced polymers including environmental effects. *Composites Part A: Applied Science and Manufacturing*, 92, 06 2016.

[16] V.P. Nguyen, O. Lloberas-Valls, M. Stroeven, and L. Sluys. Homogenization-based multiscale crack modelling: From micro-diffusive damage to macro-cracks. *Computer Methods in Applied Mechanics and Engineering*, 200:1220–1236, 02 2011.

[17] E.J. Barbero. *Finite Element Analysis of Composite Materials using AbaqusTM*. Composite Materials. Taylor & Francis, 2013.

[18] D. Garoz Gómez, F.A. Gilabert Villegas, R. Sevenois, S. Spronk, and W. Van Paepegem. Material parameter identification of the elementary ply damage mesomodel using virtual micro-mechanical tests of a carbon fiber epoxy system. *Composite Structures*, 181:391–404, 2017.

[19] A. Hyde, L. Liu, X. Cui, and J. Lua. Micromechanics-enriched finite element modeling of composite structures with fiber waviness and void defects. AIAA SciTech Forum, 01 2019.

[20] C.C. Chamis, F. Abdi, M. Garg, L. Minnetyan, H. Baid, D. Huang, J. Housner, and F. Talagani. Micromechanics-based progressive failure analysis prediction for wwfe-iii composite coupon test cases. *Journal of Composite Materials*, 47(20-21):2695–2712, 2013.

[21] R. Talreja. *Incorporating manufacturing defects in damage and failure analysis*, pages 377–390. 12 2016.

[22] H. Jiang, Y. Ren, Z. Liu, and S. Zhang. Microscale finite element analysis for predicting effects of air voids on mechanical properties of single fiber bundle in composites. *Journal of Materials Science*, 54, January 2019.

[23] K. Chowdhury, R. Talreja, and A. Benzerga. Effects of manufacturing-induced voids on local failure in polymer-based composites. *Journal of Engineering Materials and Technology*, 130, 04 2008.

[24] J. Aboudi. The response of a partially loaded composite half-space weakened by local defectsx. *International Journal of Solids and Structures*, 168, 03 2019.

[25] M. Naderi and N. Iyyer. Micromechanical analysis of damage mechanisms under tension of 0o-90o thin-ply composite laminates. *Composite Structures*, 234:111–659, 11 2019.

[26] A. Benzerga, X. Poulain, K. Chowdhury, and R. Talreja. Computational methodology for modeling fracture in fiber-reinforced polymer composites. *Journal of Aerospace Engineering*, 22, 07 2009.

[27] H. Huang and R. Talreja. Effects of void geometry on elastic properties of unidirectional fiber reinforced composites. *Composites Science and Technology*, 65:1964–1981, 10 2005.

[28] L. Zhuang and R. Talreja. Effects of voids on postbuckling delamination growth in unidirectional composites. *International Journal of Solids and Structures*, 51:936–944, 03 2014.

[29] D. Vajari, C. Gonzalez, J. Llorca, and B. Legarth. A numerical study of the influence of microvoids in the transverse mechanical response of unidirectional composites. *Composites Science and Technology*, 97, 06 2014.

[30] T. Huang and Y. Gong. A multiscale analysis for predicting the elastic properties of 3d woven composites containing void defects. *Composite Structures*, 185, 11 2017.

[31] I. Kaleel, M. Petrolo, A. Waas, and E. Carrera. Computationally efficient, high-fidelity micromechanics framework using refined 1d models. *Composite Structures*, 181, 08 2017.

[32] I. Kaleel, M. Petrolo, E. Carrera, and A. Waas. Micromechanical progressive failure analysis of fiber-reinforced composite using refined beam models. 11 2017.

[33] I. Kaleel, M. Petrolo, E. Carrera, Pineda. E.J., T.M. Ricks, B.A. Bednarcyk, and S.M. Arnold. Integration of cuf micromechanics framework into NASMAT for multiscale analysis of fiber-reinforced

composites. In ICMAMS, editor, *Proceedings of the Second International Conference on Mechanics of Advanced Materials and Structures - ICMAMS 2019, Nanjing, China.*

[34] E. Carrera, M. Cinefra, E. Zappino, and M. Petrolo. *Finite Element Analysis of Structures Through Unified Formulation.* John Wiley & Sons Ltd, 2014.

[35] I Kaleel, M Petrolo, E Carrera, and AM Waas. Computationally efficient concurrent multiscale framework for the linear analysis of composite structures. *AIAA Journal*, 57(9):4019–4028, 2019.

[36] I Kaleel, M Petrolo, E Carrera, and AM Waas. Computationally efficient concurrent multiscale framework for the nonlinear analysis of composite structures. *AIAA Journal*, 57(9):4029–4041, 2019.

[37] E. Carrera and M. Petrolo. Refined beam elements with only displacement variables and plate/shell capabilities. *Meccanica*, 47(3):537–556, 2012.

[38] R. Sevenois, G.D. Garoz, E. Verboven, S. Spronk, F. Gilabert, M. Kersemans, L. Pyl, and W. Van Paepegem. Multiscale approach for identification of transverse isotropic carbon fibre properties and prediction of woven elastic properties using ultrasonic identification. *Composites Science and Technology*, 168, 09 2018.

[39] D.C. Montgomery. *Applied Statistics and Probability for Engineers, 6th Edition.* John Wiley and Sons, Incorporated, 2013.

[40] J.M. Chambers. *Graphical Methods for Data Analysis.* CRC Press, 2018.

[41] W. Yu. An introduction to micromechanics. In *Composite Materials and Structures in Aerospace Engineering*, volume 828 of *Applied Mechanics and Materials*, pages 3–24. Trans Tech Publications Ltd, 4 2016.